



Cite this: DOI: 10.1039/d5cy00663e

# Tungsten single-atom catalysts for the efficient conversion of isobutene into highly branched liquid hydrocarbons

Abdallah F. Zedan, <sup>ab</sup> Michael Moody, <sup>a</sup> Tushar Bera, <sup>c</sup> Jeffrey H. Simpson, <sup>d</sup> Sungsik Lee, <sup>e</sup> Ahmed A. Farghaly <sup>f</sup> and M. Samy El-Shall <sup>\*a</sup>

The catalytic transformation of isobutene into branched liquid hydrocarbons is crucial for the production of reformulated gasoline and fuel additives. Conventional supported catalysts often lack high activity and selectivity toward the desired highly branched dimers and trimers in isobutene oligomerization. Here, by developing a tungsten single-atom catalyst ( $W_{SAC}$ ) atomically dispersed on a silica-doped alumina (SDA) support, we report that the  $W_{SAC}/SDA$  catalyst enables efficient and selective conversion of isobutene into highly branched  $C_8$  and  $C_{12}$  liquid olefins while suppressing the formation of heavier hydrocarbons. The atomically dispersed  $W_1-O_3$  moieties incorporated within the SDA support were synthesized *via* a high-temperature pyrolysis of a templating zinc metal-organic framework (Zn-MOF) under argon, followed by annealing in static air. The  $W_{SAC}/SDA$  catalysts with 1.6–3.7 wt% W loading exhibited single-atom dispersion ( $\sim 0.2$  nm) and outstanding performance, achieving up to 60% and 95% selectivity to branched  $C_8$  olefins at 150 °C and 250 °C, respectively, under ambient pressure. With the demonstrated high activity, selectivity, and stability, the  $W_{SAC}/SDA$  catalyst system presents a promising platform for next-generation heterogeneous catalysts for the efficient and selective upgrading of isobutene into high-performance fuel additives.

Received 4th June 2025,  
Accepted 21st August 2025

DOI: 10.1039/d5cy00663e

rsc.li/catalysis

## Introduction

Isobutene ( $[(CH_3)_2C=CH_2]$ ), a relatively undervalued light hydrocarbon commonly used in liquefied petroleum gas (LPG), has attracted interest as a feedstock for the production of value-added chemicals.<sup>1</sup> Branched liquid olefins in the  $C_8$ – $C_{12}$  range are high-value products used extensively across the petrochemical sector, particularly in the manufacture of fine chemicals and fuel additives.<sup>2</sup> The catalytic oligomerization of isobutene into branched high-molecular-weight olefins offers a sustainable route to produce high-octane aviation fuels and octane-boosting blending components for reformulated gasoline.<sup>3</sup> Isobutene oligomerization is a complex, exothermic process involving a network of parallel and sequential reactions, often leading to a wide distribution of oligomeric products including dimers ( $C_8$ ), trimers ( $C_{12}$ ), tetramers ( $C_{16}$ ),

and heavier oligomers ( $C_{20}^+$ ).<sup>4</sup> Selective isobutene dimerization is particularly desirable, yielding branched  $C_8$  olefins such as 2,4,4-trimethyl-1-pentene and 2,4,4-trimethyl-2-pentene. These  $C_8$  compounds fall within the gasoline fraction, possess high octane numbers, and can replace aromatic compounds in reformulated fuel blends.<sup>3,5</sup> Upon hydrogenation, these dimers can be converted to 2,2,4-trimethylpentane (isooctane), a clean-burning fuel component with low sulfur and aromatic content.<sup>5</sup> While  $C_{12}$  olefins are less suited for gasoline due to their low volatility,<sup>6</sup> they serve as important intermediates in the synthesis of heavy alkylates, neo-acids, dodecylbenzene, specialty solvents, and chemical intermediates for lubricants and gas oil additives.<sup>5,7</sup> Despite the commercial importance of isobutene dimers and trimers, achieving both high productivity and selectivity from isobutene oligomerization remains a major catalytic challenge.<sup>8–10</sup> A broad spectrum of catalysts has been explored for isobutene oligomerization, including aluminosilicates,<sup>5</sup> cation exchange resins,<sup>11,12</sup> acid-modified resins,<sup>13</sup> zeolites,<sup>14</sup> ionic liquids,<sup>15</sup> and various metal-based systems (e.g., Ni, Cu, Fe, W, Zn, Ti).<sup>16–21</sup> However, many of these catalysts suffer from significant drawbacks, including poor thermal stability, limited regenerability, high-pressure requirements, and undesirable side reactions that lead to ether or coke formation.<sup>4,5,13</sup> Zeolitic catalysts like zeolite beta

<sup>a</sup> Department of Chemistry, Virginia Commonwealth University, Richmond, VA 23284, USA. E-mail: elshalls2@vcu.edu

<sup>b</sup> National Institute of Laser Enhanced Science, Cairo University, Giza, 12613, Egypt

<sup>c</sup> Shell Global Solutions US Inc., 3333 HWY 6 South, Houston, TX, USA

<sup>d</sup> Department of Chemistry, University of Richmond, Richmond, VA 23173, USA

<sup>e</sup> X-ray Science Division, Argonne National Laboratory, Lemont, Illinois 60439, USA

<sup>f</sup> Chemical Sciences & Engineering Division, Argonne National Laboratory, Lemont, Illinois, 60439 USA



and ZSM-5, although widely studied, often require elevated temperatures and pressures, and are prone to rapid deactivation due to micropore blockage and coke buildup.<sup>4,5,13</sup> The elevated temperatures and pressure requirements could lead to the formation of a range of undesired products *via* uncontrolled side reactions, such as disproportionation, aromatization, and cracking.<sup>22</sup> Mesoporous amorphous aluminosilicates offer improved mass transfer but often suffer from low acidity and poor hydrothermal stability.<sup>23</sup>

Emerging single-atom catalysts (SACs) represent a promising frontier in heterogeneous catalysis including the catalytic upgrading of isobutene into liquid fuel alkene. By anchoring isolated single-atom active species on tailored supports, SACs can offer high catalytic activity, selectivity, and atom efficiency. Their well-defined coordination environments and strong metal-support interactions also enable enhanced thermal and chemical stability.<sup>24–28</sup> Despite these advantages, tungsten-based SACs for hydrocarbon transformations, especially isobutene oligomerization, remain unexplored.

Herein, we report, for the first time, on the development of a new approach for the synthesis of tungsten single-atom catalysts supported on silica-doped alumina ( $W_{SAC}/SDA$ ) for the selective transformation of isobutene into highly branched  $C_8$  and  $C_{12}$  olefins. The  $W_{SAC}/SDA$  catalysts are synthesized *via* a templating confinement strategy using a Zn-based metal-organic framework (Zn-BTC, where BTC = 1,3,5-benzene-tricarboxylate) as a templating agent.<sup>29</sup> This route enables the atomic dispersion of tungsten species ( $W_1-O_3$ ) on the SDA support following pyrolysis at 1000 °C and post-annealing in air at 700 °C. Zn-BTC is selected as the templating MOF due to its high aqueous stability, porous structure, and the relatively low boiling point of Zn (907 °C), which facilitates its complete removal during pyrolysis.<sup>30</sup> The high water stability and the cage-like pore structure of Zn-BTC provide an excellent environment for confining guest  $W^{6+}$  ions and preventing their aggregation, particularly during high-temperature treatments.<sup>31</sup> Surface acidity, crucial for olefin oligomerization,<sup>23</sup> is provided by the SDA support derived from SIRA-5, known for its favorable acidic properties compared to pure alumina.<sup>32</sup> To compare the structural characterization and catalytic activity of the  $W_{SAC}/SDA$  catalyst with conventional nanoparticle catalysts, a  $WO_3$  nanoparticle catalyst supported on SDA ( $WO_3/SDA$ ) was prepared by the same method used for the synthesis of the  $W_{SAC}/SDA$  catalysts but without the use of the Zn-BTC sacrificial MOF for the confinement of the  $W^{6+}$  ions. Structural and morphological characterization techniques including XRD, Raman spectroscopy, TEM, STEM, EDS, EXANES, EXAFS, BET,  $H_2$ -TPR,  $NH_3$ -TPD, and XPS confirmed the atomically dispersed nature of  $W_1-O_3$  moieties in the  $W_{SAC}/SDA$  catalyst, contrasting with the larger nanoparticle particles observed in the  $WO_3/SDA$  catalyst. Notably, the  $WO_3/SDA$  nanoparticle catalyst exhibited negligible isobutene conversion under the reaction

conditions (150–250 °C), underscoring the necessity of W atomic dispersion for catalytic activity. The  $W_{SAC}/SDA$  catalysts, with W loadings ranging from 1.6 to 6 wt%, demonstrated tunable activity and selectivity toward  $C_8$  and  $C_{12}$  products under ambient pressure. The 3.7 wt%  $W_{SAC}/SDA$  catalyst exhibited the highest activity and selectivity, achieving substantial yields of branched liquid olefins at both 150 °C and 250 °C while effectively suppressing the formation of heavier oligomers ( $\geq C_{16}$ ). Furthermore, the  $W_{SAC}/SDA$  catalysts showed excellent thermal stability and catalytic performance over extended periods, highlighting their potential for practical applications. The current work demonstrates the facile synthesis of a promising and eco-friendly class of tungsten single-atom supported catalysts *via* the sacrificial Zn-MOF-confinement route. The  $W_{SAC}/SDA$  catalysts are active, selective, and stable in ambient conditions, paving the way for a new family of heterogeneous tungsten single-atom catalysts for selective olefin oligomerization and fuel additive production.

## Experimental section

### Materials

Zinc nitrate hexahydrate ( $Zn(NO_3)_2 \cdot 6H_2O$ , 98%, Sigma-Aldrich), 1,3,5-benzene-tricarboxylic acid ( $H_3BTC$ , 98%, Acros Organic), ethanol (190 proof, Decon Labs), sodium hydroxide (97%, ACS reagent, Thermo Sci. Chem.), 5% silica-alumina hydrate (SIRA-5, Sasol), and sodium tungstate(vi) dihydrate ( $Na_2WO_4 \cdot 2H_2O$ , 99%, ACS reagent, Thermo Sci. Chem.).

### Synthesis of templating Zn-BTC MOF

The Zn-BTC MOF was prepared using  $Zn(NO_3)_2 \cdot 6H_2O$  and  $H_3BTC$  at room temperature according to the literature, with a slight modification.<sup>43,44</sup> An aqueous solution of NaOH (50 mL, 0.6 M) was added to a solution of  $H_3BTC$  (50 mL, 0.2 M) in ethanol under continuous stirring to form the corresponding  $Na_3BTC$ . To prepare the Zn-BTC MOF, 15 mmol of  $Zn(NO_3)_2 \cdot 6H_2O$  pre-dissolved in 20 mL deionized water was added to the  $Na_3BTC$  solution under vigorous stirring. The reaction mixture was stirred at room temperature for 30 min, and the resultant white precipitate was separated by filtration and washed twice using a water/ethanol mixture. Then, the solid product was dried in an electric oven at 60 °C for 8 h.

### Synthesis of $W_{SAC}/SDA$ catalysts

First, the 5 wt% SDA support was prepared by calcination of SIRA-5 at 700 °C for 5 h. Then, the different  $W_{SAC}/SDA$  catalysts were prepared by a facile two-step process involving the sacrifice of Zn-BTC MOF *via* high-temperature pyrolysis in an inert atmosphere, followed by an annealing of the catalysts in air. In a typical synthesis, 1 g of the pre-synthesized Zn-BTC and 1 g of the 5% SDA were dispersed in 30 mL of a water/ethanol mixed solvent by ultrasonication. Then, predetermined quantities of  $Na_2WO_4 \cdot 2H_2O$  were added to the mixture under vigorous stirring. The reaction mixture was



heated in an oil bath at 110 °C under continuous vigorous stirring until the solvent was evaporated. The resultant precipitate was pyrolyzed in a tube furnace at 1000 °C under an argon (Ar) flow for 2 h. The obtained solid was finally activated by annealing under static air in a muffle furnace at 700 °C for 5 h. A fixed heating rate of 10 °C min<sup>-1</sup> was employed for both the pyrolysis and the activation steps. The effect of tungsten (W) loading on the catalytic performance was evaluated by varying the tungsten content in the range of 1.6–6 wt%. For comparison, a 3.5 wt% WO<sub>3</sub>/SDA nanoparticle catalyst was prepared by using Na<sub>2</sub>WO<sub>4</sub>·2H<sub>2</sub>O *via* similar processes, including high-temperature pyrolysis under Ar followed by annealing in air as described above, but excluding templating Zn-BTC. The prepared WO<sub>3</sub>/SDA nanoparticle catalyst was used for comparison to reveal the effect of the templating Zn-BTC MOF on the structural, electronic, and catalytic properties of the W<sub>SAC</sub>/SDA catalysts. The experimental weight ratios of tungsten in the different samples were determined using ICP.

### Characterization

Samples were characterized using powder X-ray diffraction (XRD), Raman spectroscopy, high-resolution transmission electron microscopy (HRTEM), scanning transmission electron microscopy (STEM), electron diffraction spectroscopy (EDS), BET surface area analysis, temperature-programmed reduction (H<sub>2</sub>-TPR), temperature-programmed desorption using ammonia (NH<sub>3</sub>-TPD), and X-ray photoelectron spectroscopy (XPS).

XRD patterns were collected at room temperature using an X'Pert Philips materials research diffractometer equipped with a Cu emitter. Raman spectra were recorded using a Horiba LABRam HR evolution confocal Raman spectrometer equipped with a CCD camera as a detector and using a 532 nm laser source for excitation. HRTEM, STEM, and EDS images were acquired using JEM-F200 electron microscopes. BET surface area measurement was carried out using a Micromeritics 3Flex analyzer. H<sub>2</sub>-TPR and NH<sub>3</sub>-TPD measurements were conducted using a Micromeritics AutoChem II 2920 analyzer. XPS spectra were acquired using a PHI VersaProbe III scanning XPS microprobe. The experimental tungsten loading of the various catalysts was determined using ICP-OES. Any zinc content remaining in the three W<sub>SAC</sub>/SDA catalysts synthesized using the templating Zn-BTC was investigated using X-ray fluorescence (XRF) and inductively coupled plasma (ICP) measurements.

Extended X-ray absorption near edge structure (EXANES) and extended X-ray absorption fine structure (EXAFS) spectra of the W L<sub>3</sub>-edge were collected at beamline 12-BM-B of the Advanced Photon Source (APS, Argonne National Laboratory, USA) in transmission and fluorescence mode simultaneously by a Si (111) double-crystal monochromator. The samples were prepared as thin pellets on adhesive Kapton tape. The spectrum of a W foil was acquired simultaneously with each sample scan as a reference for energy calibration. The XAFS

spectra were averaged, background subtracted and normalized using the Athena software package.

### Catalysis measurements

The catalytic activity of the prepared samples to convert isobutene into liquid hydrocarbons was studied using a continuous-flow fixed-bed tubular reactor. In all experiments, 250 mg of the catalyst was charged into the middle of the reactor tube. Isobutene (99%, chemically pure grade, Linde, USA) was fed into the reactor in the gas phase, and the flow rate was controlled using a Brooks mass flow controller to achieve a gas hourly space velocity (GHSV) of 3000 h<sup>-1</sup>. Isobutene (IB) conversion was studied under atmospheric pressure at two different reaction temperatures of 150 °C and 250 °C for 6 h on stream. The outlet gas was passed downstream of the reactor tube to a cold trap at -20 °C to condense any liquid product.

### GC product analysis

The fraction converted from the initial isobutene was determined using an inline industrial gas chromatograph (SRI 8610 C) equipped with a thermal conductivity detector (TCD). Integral data of the isobutene peaks of chromatograms obtained for the inlet and outlet gas were used to express the isobutene concentration. The catalytic activity was expressed as a function of isobutene converted and was calculated as:

$$\% \text{Isobutene (IB) Conversion} = \frac{[\text{IB}]_{\text{in}} - [\text{IB}]_{\text{out}}}{[\text{IB}]_{\text{in}}} \times 100. \quad \text{The}$$

condensate in the cold trap was collected and analyzed using an Agilent 6890 GC-MS system, and products were identified using the attached NIST mass spectral database (library version 2). The product selectivity was calculated as the mole fraction of C<sub>8</sub> and C<sub>12</sub> in the liquid olefin mixture.

### NMR spectroscopy of liquid products

NMR spectroscopy measurements were performed to determine the compositions of the liquid samples collected from the isobutene conversion reactions over different catalysts and temperatures. NMR data were collected using a Bruker NanoBay Avance III HD 400 MHz NMR spectrometer. Samples were dissolved in deuterated chloroform, and the following NMR spectra were collected for each sample: <sup>1</sup>H 1D, <sup>1</sup>H-<sup>1</sup>H 2D COSY, <sup>1</sup>H-<sup>13</sup>C 2D HSQC, and <sup>1</sup>H-<sup>13</sup>C 2D HMB. The data were processed using MestReNova software (version 14.2.0-26256). For the 1D NMR spectra, 32k data points were collected, and this was then zero-filled to a size of 64k upon Fourier transform. The <sup>1</sup>H spectral window covered the range from -4 ppm to +16 ppm. A line broadening of 0.3 Hz was applied to the time-domain data before the Fourier transformation. 2D NMR spectra were used to determine/confirm structures and integrals of the signals in the 1D spectrum were tabulated and analyzed. The integral data were normalized based on how many hydrogens were generated in each signal. The percent composition of



each molecular component in a mixture was determined by the division of the integral-per-H in each molecule by the sum of all the integral-per-H values. The consistency of each molecular component's integrals was evaluated and used to generate compositional uncertainties.

## Results and discussion

### Single-atom catalyst synthesis strategy

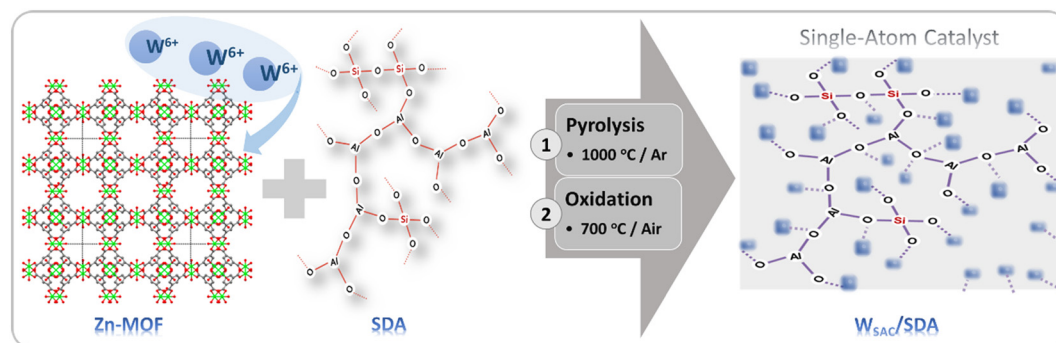
Scheme 1 illustrates the templating MOF-confinement/pyrolysis-oxidation strategy for the synthesis of  $W_{SAC}$  in the form of  $W_1-O_3$  moieties bonded to silica-doped alumina support ( $W_{SAC}/SDA$ ).

For the synthesis of the different  $W_{SAC}/SDA$  catalysts, the support material (SDA) was derived from SIRAL-5, a commercially available silica-alumina hydrate containing 5 wt% silica, *via* calcination at 700 °C for 5 hours in static air. Zn-BTC was selected as a templating MOF because of the demonstrated stability of Zn-BTC in aqueous and hydroalcoholic environments as well as the low boiling point of zinc (907 °C), which facilitates its complete removal during pyrolysis at 1000 °C. As depicted in Scheme 1, the SDA support and Zn-BTC MOF were co-dispersed in a water-ethanol solvent system using ultrasonication to ensure homogeneous mixing. Numerous studies have confirmed the high structural stability of BTC-based MOFs, particularly Zn-BTC, under aqueous or water-alcohol conditions.<sup>33,34</sup> Zn-BTC maintains its crystallinity, porosity, and framework integrity upon exposure to water, without significant degradation or collapse. Additionally, it exhibits excellent water sorption properties, making it suitable for dispersion in the solvent mixture used in this work.<sup>33,34</sup> Tungsten ions were introduced into the Zn-BTC/SDA system in the form of sodium tungstate. Vigorous stirring ensured uniform distribution of  $W^{6+}$  ions throughout the Zn-BTC/SDA suspension. This step promotes the confinement of tungsten species within the large cage-like pores of the Zn-BTC MOF, effectively preventing premature diffusion or agglomeration of  $W_{SAC}$  species during subsequent high-temperature pyrolysis. Following tungsten metal ion incorporation, the solvent was evaporated by heating the mixture at 110 °C

under continuous stirring. The resulting solid was then thoroughly washed with deionized water to remove any surface-adsorbed tungstate ions, ensuring that only W species confined within the MOF cavities remained. This washed precursor was subjected to pyrolysis at 1000 °C under an inert atmosphere (Ar), during which the Zn-BTC framework decomposed, releasing volatile Zn species and leaving behind atomically dispersed tungsten sites anchored within the SDA matrix. Finally, the pyrolyzed material was annealed in static air at 700 °C to activate the  $W_{SAC}/SDA$  catalyst. This post-treatment step may further stabilize the tungsten active sites and optimize their oxidation state, preparing the material for catalytic applications.

### Catalyst characterization

The XRD analysis (Fig. S1, SI) revealed that the templating Zn-BTC MOF exhibits diffraction peaks at  $2\theta = 8.8^\circ$ ,  $10.1^\circ$ ,  $13.5^\circ$ ,  $17.6^\circ$ ,  $18.6^\circ$ ,  $20.3^\circ$ ,  $22.1^\circ$ , and  $26.1^\circ$  typical of Zn-BTC material. These match well with both experimental and simulated patterns reported in the literature.<sup>35</sup> Fig. 1 displays the XRD patterns of the SIRAL-5, 5 wt% SDA support, 3.5 wt%  $WO_3/SDA$  nanoparticle catalyst, and the various  $W_{SAC}/SDA$  catalysts (1.6 wt%, 3.7 wt%, and 6 wt%) synthesized using the templating Zn-BTC MOF *via* high-temperature pyrolysis. The SIRAL-5 precursor displays an XRD pattern typical of the böehmite  $[AlO(OH)]$  phase, commonly used in the preparation of silica-alumina hydrates.<sup>36</sup> The XRD of the 5% SDA support synthesized by calcining SIRAL-5 at 700 °C for 5 h in static air shows diffraction peaks characteristic of the cubic  $\gamma-Al_2O_3$  phase at  $2\theta = 46.2^\circ$  and  $66.9^\circ$ .<sup>37</sup> For the  $WO_3/SDA$  nanoparticle catalyst and the 1.6%, 3.7%, and 6%  $W_{SAC}/SDA$  catalysts, the XRD patterns still show the two main  $\gamma-Al_2O_3$  peaks, with only slight shifts to  $2\theta = 46.1^\circ$  and  $66.8^\circ$  in the three  $W_{SAC}/SDA$  catalysts. Notably, no diffraction peaks attributable to tungsten oxide ( $WO_x$ ) species were detected in the  $WO_3/SDA$  nanoparticle catalyst and the  $W_{SAC}/SDA$  catalysts, even at the high tungsten loading of 6 wt%. This suggests a uniform and high dispersion of tungsten species across the SDA support surface. Similar observations have been reported for ultrasmall or single-atom catalysts.<sup>36,38</sup>



**Scheme 1** MOF-confinement of  $W^{6+}$  ions and mixing with SDA followed by pyrolysis at 1000 °C to vaporize the Zn framework and oxidation in air at 700 °C to incorporate W atoms within the SDA support.





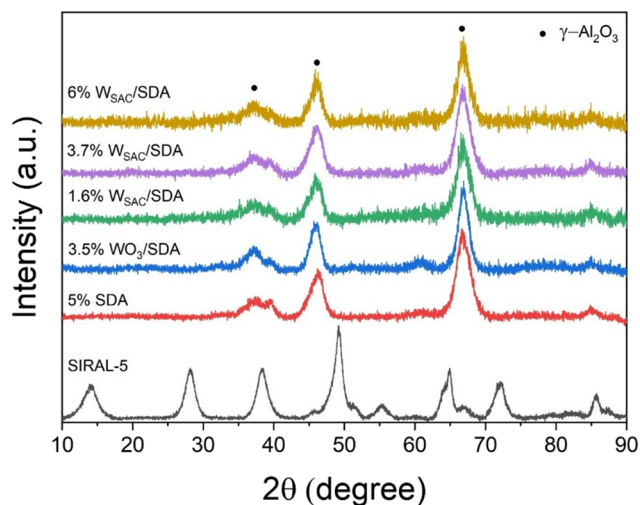


**Fig. 1** XRD patterns of the SIRAL-5, 5 wt% SDA support, 3.5 wt%  $\text{WO}_3$ /SDA nanoparticle catalyst prepared without the templating Zn-BTC MOF, and the various (1.6 wt%, 3.7 wt%, and 6 wt%)  $\text{W}_{\text{SAC}}/\text{SDA}$  catalysts prepared using the templating Zn-BTC MOF *via* high-temperature pyrolysis at 1000 °C under Ar flow, followed by annealing in static air at 700 °C.

However, minor broad bands in the  $2\theta$  range of 20–25° observed in the XRD pattern of the 6%  $\text{W}_{\text{SAC}}/\text{SDA}$  catalyst may hint at the presence of finely dispersed  $\text{WO}_3$  species, yet well-integrated and homogeneously distributed on the SDA support.<sup>38,39</sup> Importantly, no peaks corresponding to ZnO were observed in any of the  $\text{W}_{\text{SAC}}/\text{SDA}$  catalysts. Under the applied pyrolysis conditions (1000 °C, 2 h), Zn species likely evaporated due to their low boiling point (~907 °C), leaving

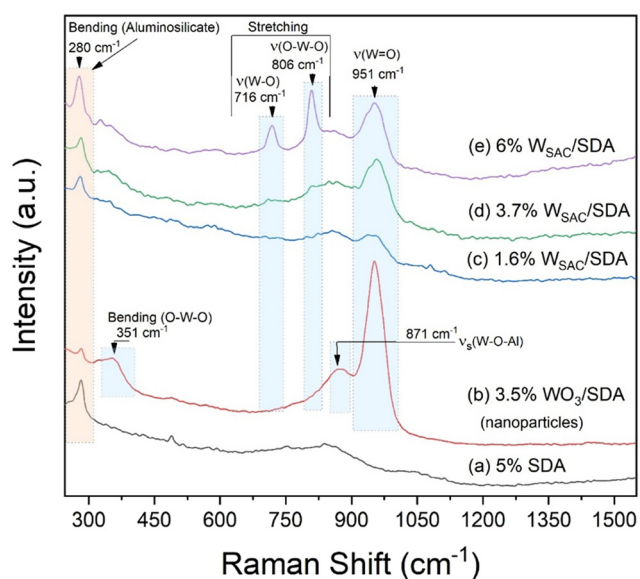


**Fig. 2** Raman spectra of (a) the SDA support prepared from SIRAL-5 at 700 °C in air for 5 h, (b) 3.5%  $\text{WO}_3$ /SDA nanoparticle catalyst prepared by a sol-gel method without using the templating Zn-MOF, and (c) 1.6 wt%, (d) 3.7 wt%, and (e) 6 wt%  $\text{W}_{\text{SAC}}/\text{SDA}$  catalysts prepared using templating Zn-BTC to confine the  $\text{W}^{6+}$  ions and incorporate the isolated  $\text{W}_1\text{-O}_3$  moieties within the SDA support.

no detectable residue in the final catalyst materials. This was confirmed by X-ray fluorescence (XRF), XPS, and ICP spectroscopy measurements, which showed negligible Zn content (0.003–0.006 wt%) in the final three  $\text{W}_{\text{SAC}}/\text{SDA}$  catalysts.

Structural elucidation of the 3.5 wt%  $\text{WO}_3$ /SDA nanoparticle catalyst and the three  $\text{W}_{\text{SAC}}/\text{SDA}$  catalysts was carried out by Raman spectroscopy as shown in Fig. 2. The Raman spectrum of the SDA support features a Raman band at ~280  $\text{cm}^{-1}$  assigned to the bending vibration of the 8-membered rings of aluminosilicate ( $\text{Si-O-Al}$ ) materials.<sup>40</sup> The spectrum of the  $\text{WO}_3$ /SDA nanoparticle catalyst (Fig. 2b) displays two broad Raman bands characteristic of symmetric ( $\nu_s$ ) and asymmetric ( $\nu_{as}$ ) stretching of  $\text{W=O}$  at 953  $\text{cm}^{-1}$  and 870  $\text{cm}^{-1}$ , respectively.<sup>41</sup> The broadening of the peaks is a result of the nanoparticle size and the interaction with the SDA support. The  $\nu_s$  ( $\text{W=O}$ ) and  $\nu_{as}$  ( $\text{W=O}$ ) bands of the  $\text{W}_{\text{SAC}}/\text{SDA}$  catalysts shift to slightly lower wavenumbers (951  $\text{cm}^{-1}$  and 860  $\text{cm}^{-1}$ , respectively) but with much weaker intensity and significantly broader features in comparison with the  $\text{WO}_3$ /SDA nanoparticle catalyst. The significant broadening and the weak intensity of the  $\nu_s$  ( $\text{W=O}$ ) and  $\nu_{as}$  ( $\text{W=O}$ ) bands are considered the characteristic Raman features of the  $\text{W}_{\text{SAC}}/\text{SDA}$  catalysts. The weak Raman features observed for the 1.6 wt%  $\text{W}_{\text{SAC}}/\text{SDA}$  are consistent with the small number of single-atom sites available for the catalyst because of the low W loading ratio (1.6 wt%). However, the highest W loading catalyst (6 wt%) displays new strong Raman bands at 806  $\text{cm}^{-1}$  and 716  $\text{cm}^{-1}$  in addition to the broad features assigned to the  $\nu_s$  and  $\nu_{as}$  of the  $\text{W=O}$  bond in the  $\text{W}_{\text{SAC}}/\text{SDA}$  catalysts. The relatively sharp bands observed at 806  $\text{cm}^{-1}$  and 716  $\text{cm}^{-1}$  are assigned to symmetric stretching and bending modes of the  $\text{W-O}$  bond in crystalline  $\text{WO}_3$ , respectively.<sup>42</sup> These bands are absent in the spectrum of the 1.6 wt%  $\text{W}_{\text{SAC}}/\text{SDA}$  catalyst, but they start to show up with very small intensities in the spectrum of the 3.7 wt%  $\text{W}_{\text{SAC}}/\text{SDA}$  catalyst as shown in Fig. 2. The observation of Raman bands due to crystalline  $\text{WO}_3$  in the 6 wt%  $\text{W}_{\text{SAC}}/\text{SDA}$  catalyst is also consistent with the XRD pattern shown in Fig. 1, which suggests the presence of finely dispersed  $\text{WO}_3$  species in this catalyst. The presence of crystalline bulk or aggregated  $\text{WO}_3$  nanoparticles within the 6 wt%  $\text{W}_{\text{SAC}}/\text{SDA}$  catalyst could diminish the expected enhanced catalytic activity of the SACs.

The morphological properties of the prepared 5% SDA support, the different  $\text{W}_{\text{SAC}}/\text{SDA}$  catalysts, and the  $\text{WO}_3$ /SDA nanoparticle catalyst were investigated using TEM, STEM, and EDS techniques. Fig. S2 presents TEM images of the 5% SDA support, synthesized *via* calcination of SIRAL-5 material at 700 °C in static air for 5 h. The SDA support predominantly exhibits elongated particles with individual particle lengths in the range of ~20–30 nm, as shown in Fig. S2(a–c). The elongated morphology along with the flake-like texture of the SDA support suggests a high surface area and an open structure that can favor metal dispersion.



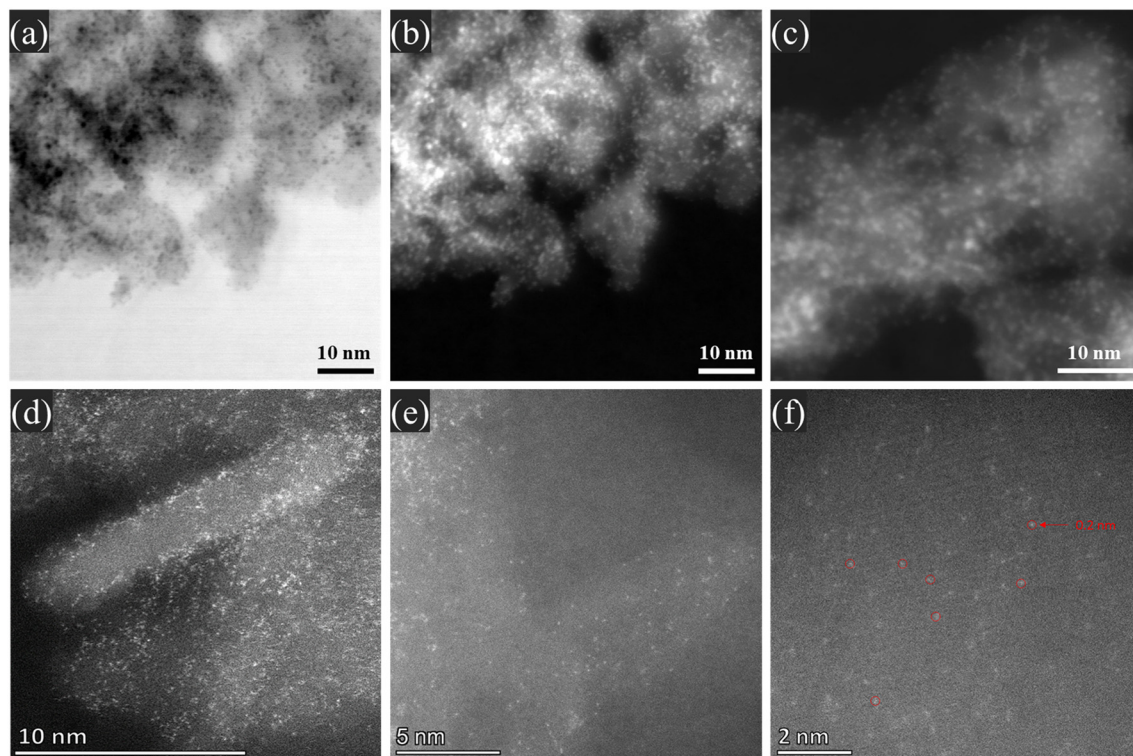


Fig. 3 (a) Dark-field and (b and c) bright-field low-resolution STEM images and (d–f) HAADF-STEM images of the 3.7 wt%  $W_{SAC}/SDA$  catalyst.

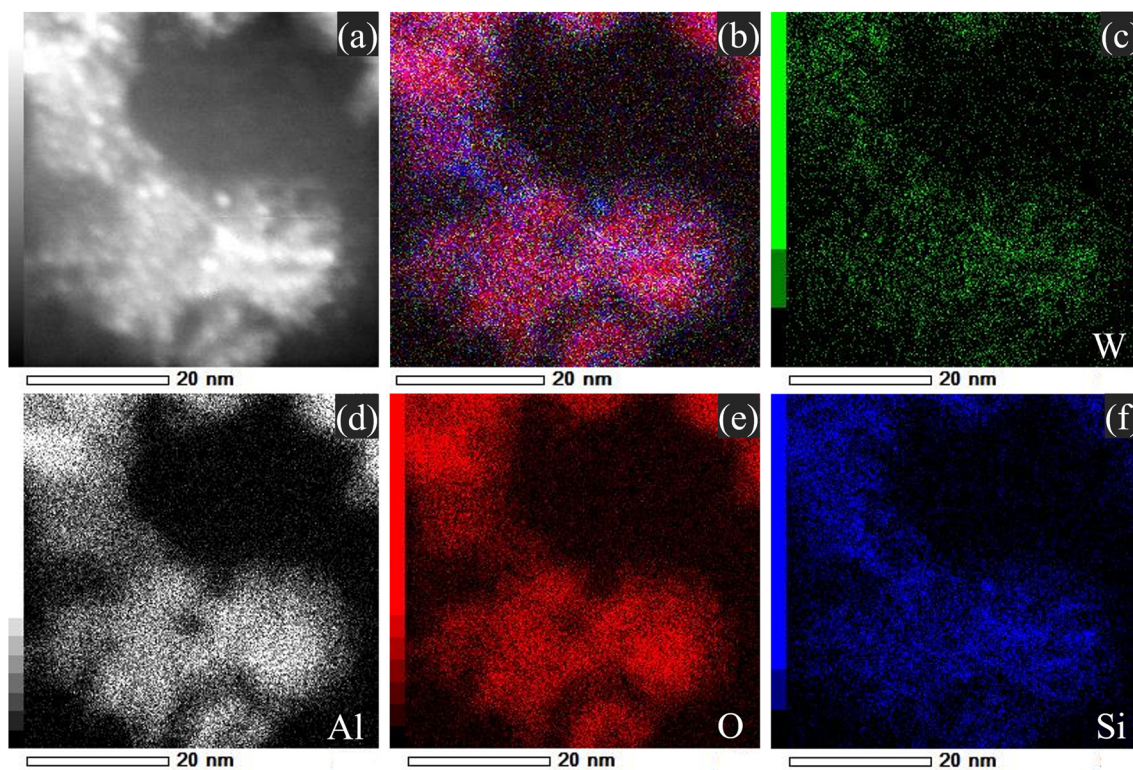


Fig. 4 (a) EDS mapping SEM image, (b) EDS layer image, and (c–f) EDS elemental mapping images of (c) tungsten, (d) aluminum, (e) oxygen, and (f) silicon of the 3.7 wt%  $W_{SAC}/SDA$  catalyst.

The morphology of the  $W_{SAC}/SDA$  catalysts prepared using templating Zn-BTC MOF was examined using TEM, STEM,

and EDS (Fig. S3, 3 and 4). The TEM images of the 1.6%, 3.7%, and 6%  $W_{SAC}/SDA$  catalysts (Fig. S3) show ultrasmall





spherical particles anchored onto the SDA support. The 1.6%  $W_{SAC}/SDA$  (Fig. S3a–c) and 3.7%  $W_{SAC}/SDA$  (Fig. S3d–f) samples appear as well-dispersed particles with uniform distribution over the SDA support. On the other hand, the TEM images of the 6%  $W_{SAC}/SDA$  sample (Fig. S3g–i) show more compact and darker structures, indicating partial aggregation likely due to the higher loading of tungsten species. The large dark regions indicate that particle coalescence and agglomerated clusters are present simultaneously with a small fraction of the single-atom sites, in agreement with the Raman results shown in Fig. 2. The low-resolution STEM images and high-resolution HAADF-STEM images of the 3.7%  $W_{SAC}/SDA$  sample are shown in Fig. 3. The dark- and bright-field STEM images of the 3.7%  $W_{SAC}/SDA$  sample (Fig. 3a–c) reveal the successful decoration of the SDA support with W single atoms. The HAADF-STEM images of the 3.7%  $W_{SAC}/SDA$  (Fig. 3d–f) show W single-atom moieties with an average size of  $\sim 0.2$  nm in diameter. These single-atom moieties are isolated and well dispersed within the domains of the elongated SDA particles. The ultrasmall size and dispersion of the bright dots representing high-atomic-number tungsten species confirm the single-atom nature of tungsten and its homogeneous distribution across the SDA support. The EDS images displayed in Fig. 4 show the spatial distribution of the W, Al, O, and Si elements of the 3.7%  $W_{SAC}/SDA$  sample. The EDS mapping reveals the homogenous dispersion of the tungsten species within the SDA matrix, with tungsten predominantly located near the SDA support domains. Overall, the XRD and Raman results (Fig. 1 and 2) and the morphological analyses (Fig. 3, 4 and S3) confirm that the  $W_{SAC}/SDA$  catalysts (particularly the 1.6% and the 3.7% catalysts) synthesized using templating Zn-BTC MOF *via* controlled pyrolysis and annealing processes contain well-dispersed single-atom tungsten moieties anchored evenly onto the SDA support. On the other hand, the TEM image of the 3.5%  $WO_3/SDA$  nanoparticle catalyst (Fig. S4) that was prepared without the Zn-BTC MOF shows spherical nanoparticles with an average size in the range of 5–10 nm.

This demonstrates the critical role of the Zn-BTC MOF in obtaining the SAC catalyst.

### EXANES and EXAFS measurements

To confirm the atomic local structure of the W single-atom catalyst, W  $L_3$ -edge EXANES and EXAFS measurements were conducted on the 1.6 wt%, 3.7 wt%, and 6.0 wt%  $W_{SAC}/SDA$  samples. Data from tungsten metal foil ( $W^0$ ) and bulk  $WO_3$  ( $W^{6+}$ ) were collected as standard references. Fig. 5 and S5 display the normalized W  $L_3$ -edge XANES spectra, plots for absorption edge energy ( $E_0$ ) determination from the zero-crossing of the second derivative,  $k^3$ -weighted Fourier transform (FT) of the EXAFS spectra of 1.6–6.0%  $W_{SAC}/SDA$ , bulk  $WO_3$ , and reference W metal samples, and a selected fitting of the EXAFS spectrum of the 3.7%  $W_{SAC}/SDA$  sample. The normalized W  $L_3$ -edge XANES spectra of the samples, including samples labeled as 1.6 wt%, 3.7 wt%, and 6 wt% along with commercial  $WO_3$  and W foil are presented in Fig. 5a. The spectra for the three  $W_{SAC}$  catalysts exhibit a prominent white-line feature whose shape and intensity are comparable to that of the  $WO_3$  reference and markedly different from the W foil. This high white-line intensity, arising from electron transitions from the  $2p_{3/2}$  core level to unoccupied W 5d states, is characteristic of tungsten in a high oxidation state with significant covalent character in its bonding. The absorption edge energy ( $E_0$ ), determined from the zero-crossing of the second derivative shown in Fig. S5a, is a sensitive probe of the tungsten oxidation state. The  $E_0$  values were 10 209.26 eV for sample 1.6 wt%, 10 209.19 eV for 3.7 wt%, 10 209.19 eV for 6.0 wt%, and 10 207.00 eV for metallic W foil, while the commercial  $WO_3$  reference exhibited an  $E_0$  of 10 209.25 eV. The values of  $E_0$  for the  $W_{SAC}/SDA$  samples with 1.6–6.0 wt% W closely align with that of the bulk  $WO_3$ , suggesting that the tungsten centers in these samples predominantly exist in the hexavalent state ( $W^{6+}$ ). In contrast, the W foil shows a substantially lower  $E_0$  (10 207.00 eV), characteristic of metallic tungsten. These results imply that the 1.6 wt%, 3.7 wt%, and 6.0 wt% samples

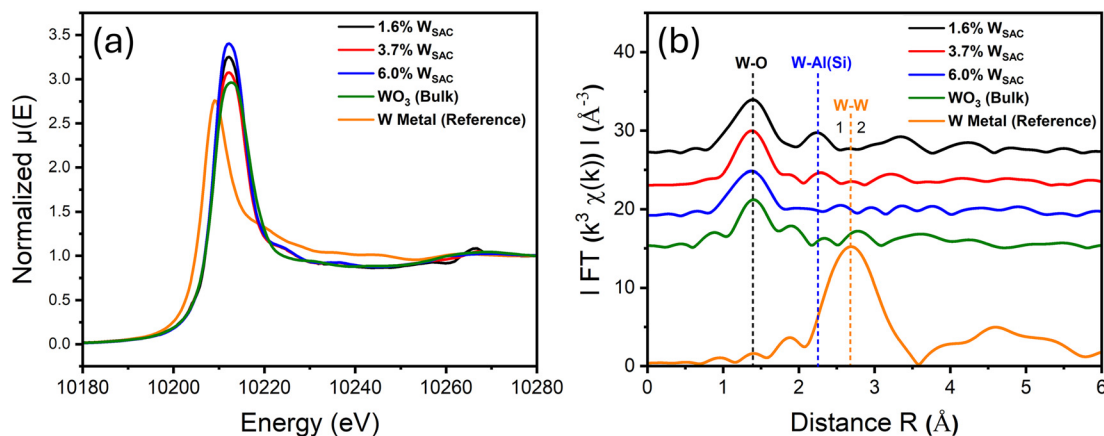


Fig. 5 (a) Normalized W  $L_3$ -edge X-ray absorption near-edge structure (XANES) spectra and (b)  $k^3$ -weighted Fourier transform (FT) of the EXAFS spectra of 1.6–6.0%  $W_{SAC}/SDA$ , bulk  $WO_3$ , and reference W metal samples.



have undergone full oxidation during synthesis, leading to a W oxidation state comparable to that of  $\text{WO}_3$ . The subtle difference in  $E_0$  ( $\Delta E = 0.07$  eV) between the 3.7 wt% and the 6.0 wt% catalysts, relative to the 1.6 wt%, may reflect slight variations in the local coordination environment or degree of structural distortion, which is explored further *via* EXAFS analysis.<sup>43–46</sup> The local coordination environment around the W atoms was investigated using extended X-ray absorption fine structure (EXAFS) analysis, and fitting was performed in *R*-space. The  $k^3$ -weighted Fourier transform (FT) of the EXAFS spectra of the different samples and sample fitting of the 3.7 wt%  $\text{W}_{\text{SAC}}/\text{SDA}$  are shown in Fig. 5b and S5b, respectively. The main fitting parameters for the EXAFS spectra are listed in Table S1. The FT-EXAFS spectrum for the 1.6 wt% W sample is characterized by scattering paths corresponding to W–O and W–Si/Al shells. The W–O coordination number was estimated to be 2.55, indicating a significantly under-coordinated environment compared to ideal  $\text{WO}_3$ , which typically exhibits sixfold W–O coordination in distorted octahedra. In addition, a W–Al shell with a coordination number of 2.37 was observed, implying partial substitution or interaction with aluminum species, possibly originating from the support or matrix. This deviation from a pure W–O network suggests that tungsten is in a highly disordered environment or at the interface with Al-containing phases. Critically, the FT-EXAFS spectrum for the 1.6 wt% W sample shows a complete absence of a W–W scattering path, which is the definitive signature of atomically dispersed species. This result illustrates that the 1.6 wt% W sample is a single-atom catalyst composed of isolated  $\text{W}^{6+}$  sites.<sup>43–46</sup> The spectrum of the 3.7 wt%  $\text{W}_{\text{SAC}}/\text{SDA}$  sample, which demonstrated the highest catalytic performance, is largely similar, indicating that it is also composed predominantly of isolated, atomically dispersed  $\text{W}^{6+}$  atoms, with a W–O coordination number of 2.39 and W–Al of 2.35. However, a careful inspection of its spectrum reveals a small feature corresponding to W–W scattering. Quantitative fitting of the EXAFS data (Table S1) for the 3.7 wt%  $\text{W}_{\text{SAC}}/\text{SDA}$  sample yields a W–W coordination number of 0.14. Although this low W–W coordination number could suggest the presence of a minor fraction of W–W dimers or ultrasmall atomic clusters alongside the predominant single-atom sites, it is worth noting that the associated uncertainty is relatively high, which limits definitive interpretation. This unique atomic structure (single atoms + dimers or ultrasmall clusters) is likely a key factor in its enhanced catalytic activity. Upon increasing the loading to 6.0 wt% W, the intensity of the W–W scattering peak in the EXAFS spectrum becomes more pronounced. This signifies a greater degree of tungsten aggregation into larger structurally disordered clusters or nanoparticles, which correlates with the observed decrease in catalytic activity compared to the 3.7 wt% sample. This is consistent with the EXAFS characterization of single-atom catalysts, which indicates that a significant fraction of clusters including metallic and oxidized metallic clusters can coexist with the SAC active sites.<sup>46</sup> The observed trend of

increasing the intensity of the W–W scattering peak in the EXAFS spectrum with increasing the wt% loading of W in the prepared catalysts suggests that while a minor population of W dimers is beneficial as in the 3.7 wt%  $\text{W}_{\text{SAC}}/\text{SDA}$  sample, further clustering is detrimental to the catalytic performance as in the 6.0 wt% sample. The best-fit parameters for all samples (Table S1) show W–O coordination numbers of  $\sim 2.4$ – $2.6$ , which are significantly lower than the sixfold coordination in bulk  $\text{WO}_3$ . This under-coordination is consistent with highly dispersed  $\text{W}^{6+}$  species anchored to the surface of the SDA support, where they form strong interactions with both oxygen, silicon, and aluminum sites of the support.<sup>43–46</sup> Based on the EXANES and EXAFS, the single-atom catalyst features were confirmed for the 1.6 wt% and 3.7 wt%  $\text{W}_{\text{SAC}}/\text{SDA}$  samples following the TEM results, and the single-constituent site in  $\text{W}_{\text{SAC}}$  was identified as  $\text{W}^{6+}$ .

### Textural and surface properties

The textural and surface properties, including surface area, pore volume, reducibility, and chemical oxidation state properties, were studied for the 3.7%  $\text{W}_{\text{SAC}}/\text{SDA}$  catalyst, which demonstrated the highest catalytic activity. Fig. 6 compares the nitrogen ( $\text{N}_2$ ) adsorption/desorption isothermal plots (Fig. 6a) and BJH adsorption  $\text{dV/dD}$  pore size distribution plots (Fig. 6b) of the 3.7%  $\text{W}_{\text{SAC}}/\text{SDA}$  catalyst to those of the 5% SDA support. The  $\text{N}_2$  adsorption/desorption isotherm of the 3.7%  $\text{W}_{\text{SAC}}/\text{SDA}$  (Fig. 6a) exhibits an isotherm similar to that of the 5% SDA and is typical of mesoporous materials. The SDA support exhibited a specific surface area (SSA) of  $347 \text{ m}^2 \text{ g}^{-1}$ , similar to values reported in the literature for silica-doped alumina.<sup>47</sup> The loading of 3.7%  $\text{W}_{\text{SAC}}$  onto the 5% SDA using templating Zn-BTC MOF and consecutive processes of controlled pyrolysis and annealing resulted in a *ca.* 18% increase of SSA from  $347 \text{ m}^2 \text{ g}^{-1}$  for SDA to  $411 \text{ m}^2 \text{ g}^{-1}$  for 3.7%  $\text{W}_{\text{SAC}}/\text{SDA}$ . On the other hand, the average pore width of the 5% SDA support is *ca.* 7.5 nm, while the 3.7%  $\text{W}_{\text{SAC}}/\text{SDA}$  catalyst exhibits a pore width distribution in the range of 3 to 7.5 nm (Fig. 6b). Such a decrease in the range of pore width distribution implies that the tungsten single-atom constituents could fill the pores of the mesoporous SDA matrix, resulting in a narrower mesoporous distribution. The higher SSA and larger volume of the small pore width distribution (3–7 nm) for the 3.7%  $\text{W}_{\text{SAC}}/\text{SDA}$  catalyst confirm the presence of the tungsten single-atom moieties.

Further information on hydrogen consumption and reducibility for selected samples was obtained by  $\text{H}_2$ -TPR. Fig. S6 displays the  $\text{H}_2$ -TPR profiles of 5% SDA and 3.7%  $\text{W}_{\text{SAC}}/\text{SDA}$  samples in the temperature range of 100–900 °C. For the SDA support, no hydrogen consumption/reduction peaks were observed up to 900 °C due to the irreducibility and high stability of the alumina support.<sup>48</sup> The 3.7%  $\text{W}_{\text{SAC}}/\text{SDA}$  catalyst shows two prominent reduction peaks denoted  $\alpha$  and  $\beta$  centered around 440 °C and 795 °C, respectively, which are ascribed to the reduction of the SDA-supported





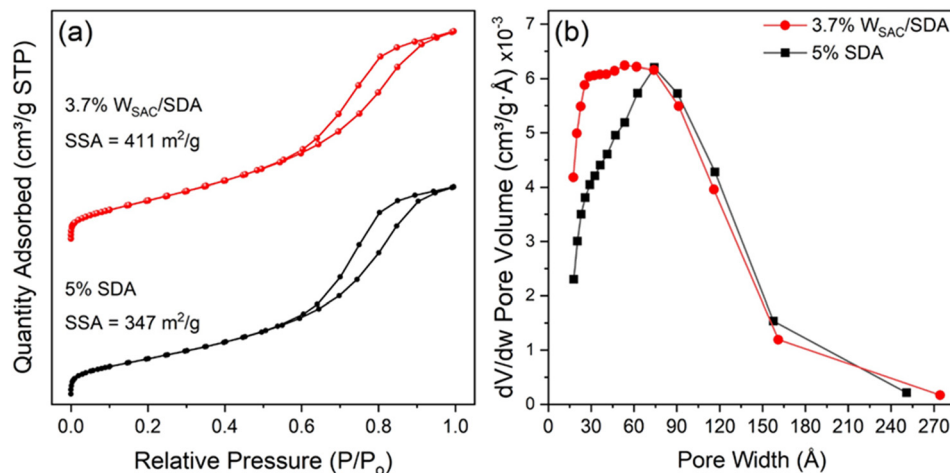


Fig. 6 (a) Nitrogen (N<sub>2</sub>) adsorption/desorption isothermal plots and (b) BJH adsorption dV/dD pore size distribution plots of the 5% SDA support and the 3.7% W<sub>SAC</sub>/SDA catalyst.

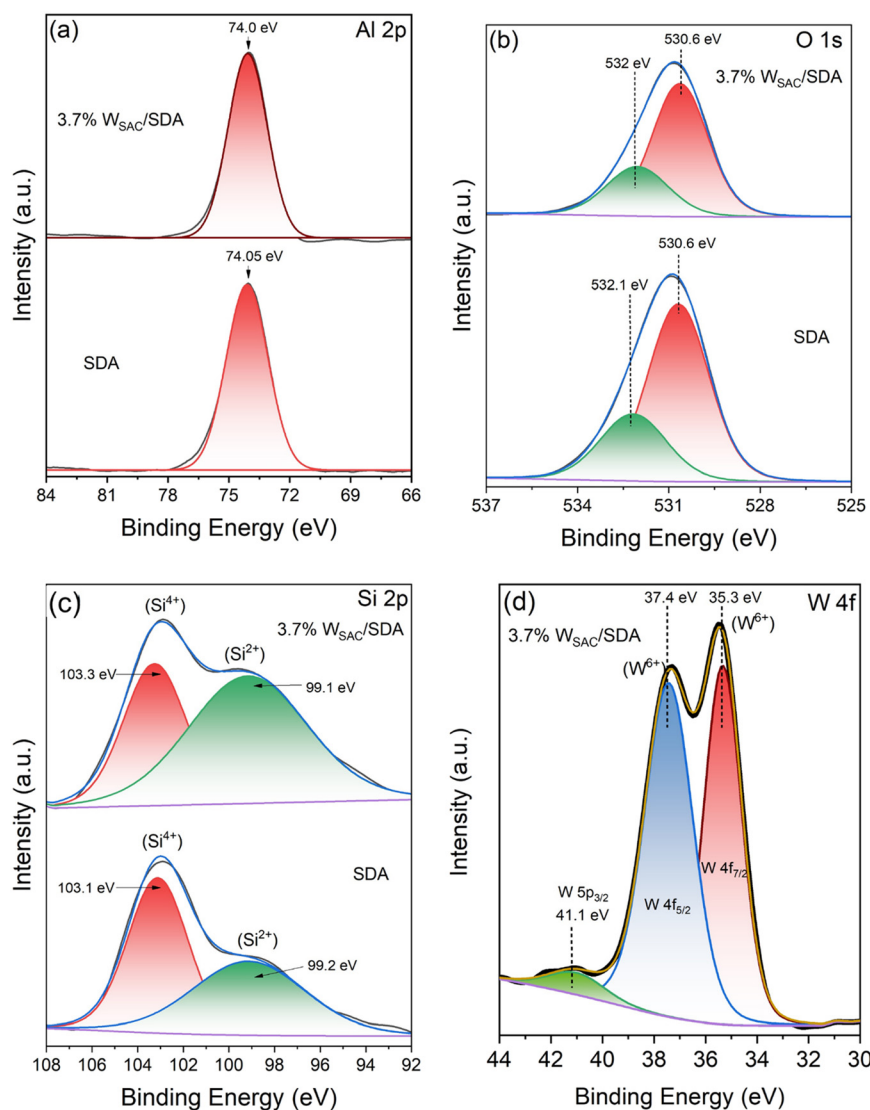


Fig. 7 High-resolution XPS spectra of (a) Al 2p, (b) O 1s, and (c) Si 2p elements of the 5% SDA support and the 3.7% W<sub>SAC</sub>/SDA catalyst, and (d) W 4f element of the 3.7% W<sub>SAC</sub>/SDA catalyst.



$W_{SAC}$  catalyst present as  $W_1-O_3$  moieties. The  $H_2$ -reduction peak at 440 °C could be attributed to the reduction of  $WO_3$  ( $W^{6+}$ ) to  $WO_{3-x}$  ( $W^{5+}$ ), while the higher-temperature reduction peak at 795 °C could be assigned to the reduction of  $WO_{3-x}$  ( $W^{5+}$  and  $W^{6+}$ ) to  $WO_2$  ( $W^{4+}$ ).<sup>49</sup> Therefore, the  $H_2$ -TPR results confirm that  $W_{SAC}$  species exist as  $W_1-O_3$  moieties. It is worth noting that the initial reduction temperature for our 3.7%  $W_{SAC}/SDA$  catalyst (440 °C) is lower by >180 °C compared to the  $H_2$ -reduction temperature of bulk  $WO_3$  (627 °C) reported by Li *et al.*<sup>49</sup> The decrease in the initial reduction temperature could be explained based on the single-atom features of the 3.7%  $W_{SAC}/SDA$  catalyst and the availability of readily reducible  $W_{SAC}$  moieties on the surface.<sup>50</sup>

The ammonia temperature-programmed desorption ( $NH_3$ -TPD) properties of the 5% SDA support and the  $W_{SAC}/SDA$  catalysts were evaluated, and  $NH_3$ -TPD profiles are presented in Fig. S7. The  $NH_3$ -TPD profiles show similar ammonia desorption behavior between the different  $W_{SAC}/SDA$  catalysts and the SDA support. The  $W_{SAC}/SDA$  with different loadings (1.6–6%) did not express significant acidity, and this is why no higher oligomers or polymers were formed in the catalytic conversion of isobutene, which is one of the desired features of the developed new catalyst. The 6%  $W_{SAC}/SDA$  catalyst shows slightly higher acidity as indicated by the  $NH_3$ -TPD at 800 °C, which infers the relatively low catalytic conversion of isobutene over the 6%  $W_{SAC}/SDA$  compared to the 1.6% and 3.7%  $W_{SAC}/SDA$  catalysts.

The surface chemical states of the 5% SDA, 3.7%  $W_{SAC}/SDA$ , and 3.5%  $WO_3/SDA$  samples were analyzed by XPS. The high-resolution XPS scans of the Al 2p, O 1s, and Si 2p elements of the 5% SDA and 3.7%  $W_{SAC}/SDA$  samples and the W 4f element of 3.7%  $W_{SAC}/SDA$  are illustrated in Fig. 7. Both SDA and 3.7%  $W_{SAC}/SDA$  present a main Al 2p peak (Fig. 7a) centered around a binding energy (BE) of ~74 eV, indicating the O–Al–O bond.<sup>48</sup> In light of the information obtained from Fig. 7b, the XPS spectra of O 1s of SDA and 3.7%  $W_{SAC}/SDA$  fitted by a Lorentzian–Gaussian deconvolution display dual peaks for different lattice and adsorbed oxygen species. The main peaks at BE ~530.6 eV elucidate the lattice oxygen involved in the metal–oxygen bond, while the shoulder peaks at a higher BE of ~532 eV are ascribed to adsorbed oxygen species such as hydroxylated surface oxygen.<sup>50</sup> As a comparison, Si 2p (Fig. 7c) of SDA and 3.7%  $W_{SAC}/SDA$  show similar XPS profiles with two peaks centered around 103.1 eV (103.3 eV) and 99.2 eV (99.1 eV) for SDA (3.7%  $W_{SAC}/SDA$ ) corresponding to fully oxidized silicon ( $Si^{4+}$ ,  $SiO_2$ ) and partially oxidized silicon ( $Si^{2+}$ ,  $SiO$ ), respectively.<sup>51</sup> For the 3.7%  $W_{SAC}/SDA$  catalyst, a greater sub-stoichiometric-to-stoichiometric ( $Si^{2+}/Si^{4+}$ ) peak ratio was observed. This can be understood based on the sharing of oxygen between tungsten and support (Si–O–W) as a result of the incorporation of tungsten ions.<sup>37</sup> As displayed in Fig. 7d, the deconvoluted XPS spectrum of W 4f of 3.7%  $W_{SAC}/SDA$  shows two major peaks at a BE of 35.3 eV ( $W 4f_{7/2}$ ) and 37.4 eV ( $W 4f_{5/2}$ ) and a small additional peak at 41.1 eV attributed

to  $W 5p_{3/2}$ .<sup>52</sup> The two major peaks (35.3 and 37.4 eV) are ascribed to the  $W^{6+}$  ions of  $WO_6$  octahedra, elucidating the existence of the monoclinic  $WO_3$  structure.<sup>53</sup> Following the  $H_2$ -TPR results (Fig. S6), the XPS studies further confirm the existence of  $W_{SAC}$  species in the oxide form ( $W_1-O_3$ ).

High-resolution XPS spectra of the Al 2p, O 1s, Si 2p, and W 4f regions for the comparison 3.5%  $WO_3/SDA$  nanoparticle catalyst sample are presented in Fig. S8. Overall, the XPS features of the 3.5%  $WO_3/SDA$  nanoparticle catalyst nearly resemble those observed for the  $W_{SAC}/SDA$  catalysts. The Al 2p region shows a single peak centered at a binding energy (BE) of 74.0 eV, indicative of tetrahedrally or octahedrally coordinated  $Al^{3+}$  species in the alumina matrix. The O 1s spectrum exhibits a dominant peak at ~530.7 eV, corresponding to lattice oxygen, as discussed previously. The Si 2p spectrum is deconvoluted into two distinct peaks centered at approximately 103.3 eV and 99.1 eV, which can be attributed to  $Si^{4+}$  in Si–O–Si (silica) and potentially Si–O–W environments ( $Si^{2+}$ ), respectively. In the W 4f region, the spectrum reveals two primary peaks located at 35.3 eV ( $W 4f_{7/2}$ ) and 37.4 eV ( $W 4f_{5/2}$ ), characteristic of tungsten in the  $W^{6+}$  oxidation state, as expected for  $WO_3$  species. However, two small peaks appear at 30.7 eV and 41.1 eV, corresponding to metallic tungsten and  $W 5p_{3/2}$  states, respectively.<sup>54</sup> These XPS results of the 3.5%  $WO_3/SDA$  nanoparticle catalyst confirm the presence of both oxidized and trace metallic tungsten species on the SDA support. Overall, the XPS results shown in Fig. 7 and S8 reveal the absence of the W–W features in the 3.7%  $W_{SAC}/SDA$  catalyst compared to the 3.5%  $WO_3/SDA$  nanoparticle catalyst which shows small metallic tungsten features. In addition, the 3.7%  $W_{SAC}/SDA$  catalyst demonstrated stronger interaction with the SDA support, as indicated by the relatively higher proportions of the  $Si^{2+}$

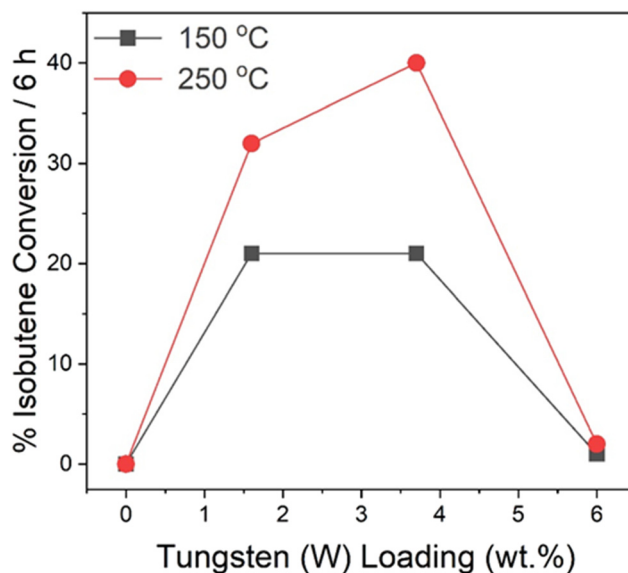


Fig. 8 Plots of % average isobutene conversion as a function of tungsten loading after 6 h at 150 °C and 250 °C under fixed GHSV and WHSV of 3000  $h^{-1}$  and 12 000  $cm^3 g^{-1} h^{-1}$ , respectively.



species because of pronounced oxygen sharing with  $W_{SAC}$  species.

### Catalyst evaluation

The activity of the prepared catalysts for isobutene conversion was studied using a continuous-flow fixed-bed catalytic reactor under atmospheric pressure. The effects of temperature and tungsten loading on the catalytic performance were investigated by employing two reaction temperatures (150 °C and 250 °C) for 6 h on the stream, utilizing 1.6%, 3.7%, and 6%  $W_{SAC}/SDA$  catalysts under fixed GHSV and WHSV of 3000  $h^{-1}$  and 12 000  $cm^3 g^{-1} h^{-1}$ , respectively. For comparison, the activity of the SDA support was studied, and no isobutene conversion or liquid hydrocarbon production was observed at the two reaction temperatures of 150 °C and 250 °C. Fig. 8 compares the average isobutene conversion as a function of catalyst loading at 150 °C and 250 °C for 6 h on stream under fixed GHSV and WHSV of 3000  $h^{-1}$  and 12 000  $cm^3 g^{-1} h^{-1}$ , respectively. Detailed plots of temporal isobutene conversion as a function of time over the different catalysts, 1.6%, 3.7%, and 6%  $W_{SAC}/SDA$  catalysts, at 150 °C and 250 °C under fixed GHSV and WHSV for 6 h are displayed in Fig. S9 and S10. The 1.6% and 3.7%  $W_{SAC}/SDA$  catalysts exhibited similar catalytic performance at 150 °C, achieving an average isobutene conversion of 20% and 21%, respectively, after 6 h on stream. Upon increasing the reaction temperature to 250 °C, the catalytic performance of both the 1.6% and the 3.7%  $W_{SAC}/SDA$  was enhanced by a half-fold and a onefold increase, respectively, demonstrating an average isobutene conversion of 32% for the 1.6%  $W_{SAC}/SDA$  and 41% in the case of the 3.7%  $W_{SAC}/SDA$ . On the other hand, the highest-loading catalyst (6%  $W_{SAC}/SDA$ ) exhibited suppressed catalytic activity, achieving only 1% and 2% isobutene conversion at 150 °C and 250 °C, respectively. Fig. S11 shows a plot of the volume of liquid products obtained following isobutene conversion for 6 h as a function of tungsten loading at 150 °C under fixed GHSV and WHSV. The rate of liquid production at 150 °C was in the order of 3.7%  $W_{SAC}/SDA > 1.6\% W_{SAC}/SDA > 6\% W_{SAC}/SDA$ . The volumes of the liquid products that were collected at 150 °C after 6 h on stream were 6 ml, 5 ml, and 0.5 ml for the 3.7%, 1.6%, and 6%  $W_{SAC}/SDA$  catalysts, respectively. The results of isobutene conversion and the rate of liquid production (Fig. 8 and S9–S11) reveal the dependence of the catalytic performance of the supported  $W_{SAC}$  catalysts on the textural and surface characteristics of the catalysts. Among those, the most probable is the size and dispersion, known to be influential for heterogeneous gas–solid reactions, because the 6% catalyst showed larger density and some surface agglomerates as revealed by TEM images (Fig. S3g–i). The highest conversion of isobutene (41%) and largest liquid production rate (1  $ml min^{-1}$ ) were obtained using the 3.7%  $W_{SAC}/SDA$  catalyst at the highest reaction temperature of 250 °C after 6 h (Fig. S10 and S11). Further increase in the W loading to 6%

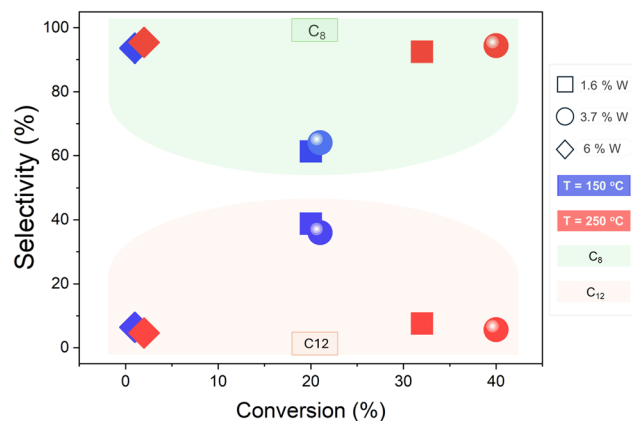


Fig. 9 Plots of average isobutene conversion (%) versus selectivity (%) toward  $C_8$  and  $C_{12}$  olefins produced using  $W_{SAC}/SDA$  catalysts (1.6%, 3.7%, and 6% W) following 6 h of isobutene oligomerization at 150 °C and 250 °C under fixed GHSV and WHSV of 3000  $h^{-1}$  and 12 000  $cm^3 g^{-1} h^{-1}$ , respectively.

resulted in a deterioration of the catalytic performance regarding both catalytic conversion and liquid hydrocarbon production.

Fig. S12 shows the plots of selectivity to  $C_8$  and  $C_{12}$  olefin products for different  $W_{SAC}/SDA$  catalysts at 150 °C and 250 °C, and Fig. 9 presents plots of average % isobutene conversion versus selectivity toward  $C_8$  and  $C_{12}$  olefins produced using  $W_{SAC}/SDA$  catalysts (1.6%, 3.7%, and 6% W) following isobutene oligomerization for 6 h at 150 °C and 250 °C under fixed GHSV and WHSV. Overall, the catalytic conversion of isobutene over different  $W_{SAC}/SDA$  catalysts resulted in the formation of a mixture of two liquid hydrocarbon products, namely dimers ( $C_8$ ) and trimers ( $C_{12}$ ), with different proportions at the reaction temperatures of 150 °C and 250 °C. No oligomers with high molecular weight ( $>C_{12}$ ) were detected at both reaction temperatures of 150 °C and 250 °C. The 1.6% and 3.7%  $W_{SAC}/SDA$  catalysts showed similar olefin product distribution with a selectivity of  $>60\%$  to dimers and  $>35\%$  to trimers at 150 °C compared to the selectivity of  $>90\%$  to dimers and  $>5\%$  to trimers at 250 °C. At 150 °C, catalytic activity is strongly influenced by W loading. The 3.7% W catalyst exhibits a slightly better  $C_8$  selectivity (64%) and lower  $C_{12}$  selectivity (36%) than the 1.6% counterpart that showed  $C_8$  selectivity of 64% and  $C_{12}$  selectivity of 39%. When the reaction temperature was increased to 250 °C, both the 1.6% and the 3.7%  $W_{SAC}/SDA$  catalysts resulted in favored formation of dimer products, demonstrating nearly a half-fold increase of  $C_8$  selectivity and a  $\sim 5$ – $6$ -fold decrease of the  $C_{12}$  selectivity. In addition to the high isobutene conversion, the 3.7%  $W_{SAC}/SDA$  catalyst also showed slightly better  $C_8$  selectivity at 250 °C. The  $C_8$  and  $C_{12}$  selectivity percentages for the 3.7%  $W_{SAC}/SDA$  were 94% and 6%, compared to 92% and 8% in the case of the 1.6%  $W_{SAC}/SDA$ , respectively. On the other hand, the high-loading catalyst (6%  $W_{SAC}/SDA$ ) led mainly to the formation of dimers at both 150 °C and 250 °C. The selectivity to the  $C_8$  and  $C_{12}$





products was 94% and 6% at 150 °C compared to 95% and 5% at 250 °C. The very low isobutene conversion (1–2%) of the 6%  $W_{\text{SAC}}/\text{SDA}$  catalyst at 150–250 °C shows that the high W loading led to catalyst deactivation due to sintering and the loss of single-atom dispersion consistent with the EXAFS results shown in Fig. 5. In contrast, the relatively high isobutene conversion and  $C_8$  selectivity in the case of 3.7% W at both 150 °C and 250 °C indicate more favorable active site density and accessibility. At the relatively low temperature of 150 °C, the dimers produced in the gas–solid reaction could partly be retained on the catalyst surface, thus reacting with isobutene and giving rise to heavier olefins (trimers). On the other hand, the increased temperature of 250 °C could favor the liberation of the produced dimers rather than retaining them on the catalyst surface, thus increasing selectivity to  $C_8$  products.<sup>5</sup> Overall, increasing the reaction temperature from 150 °C to 250 °C enhances conversion by 12–19% for the 1.6% and 3.7% W catalysts, and significantly shifts the product distribution toward  $C_8$  olefins. Additionally,  $C_{12}$  formation is strongly suppressed at higher reaction temperature across all catalysts, indicating that elevated thermal input favors selective dimerization while minimizing over-oligomerization side reactions. The increase of the W loading from 1.6% to 3.7% did not alter the catalyst's activity toward dimerization and trimerization of isobutene. However, a further increase of W loading to 6% resulted in a substantial shift of the product to dimers and a diminished activity toward trimer production as indicated by the low selectivity (6%) to  $C_{12}$  at 150 °C, where the other two lower-loading catalysts (1.6% and 3.7%) demonstrated 6-fold higher production of  $C_8$  products.

Although the selectivity–conversion plots (Fig. 9) contain only three different wt% W loading catalysts (1.6%, 3.7% and 6%), they can still establish the general trend of enhanced activity and selectivity towards the  $C_8$  dimer products (>90% at 250 °C) of the single-atom catalysts (1.6% and 3.7%  $W_{\text{SAC}}/\text{SDA}$ ) and the decreased activity of the highest W loading catalyst (6%) due to sintering and tungsten aggregation into larger clusters resulting in the loss of the critical single-atom dispersion features as confirmed by the EXAFS results shown in Fig. 5.

As previously discussed, the catalytic conversion of isobutene over  $W_{\text{SAC}}/\text{SDA}$  catalysts with varying tungsten loadings led to the formation of  $C_8$  (dimers) and  $C_{12}$  (trimers) olefins, with product selectivity influenced by both reaction temperature and W content. Notably, despite variations in catalyst composition and temperature, the nature of the products remained consistent across all tested catalysts. Specifically, two isomeric dimers and two isomeric trimers were consistently observed in all cases. Sample gas chromatograms of the liquid-phase products, presented in Fig. S13, illustrate the retention times and relative peak intensities of the  $C_8$  and  $C_{12}$  olefins formed during isobutene oligomerization over the 3.7%  $W_{\text{SAC}}/\text{SDA}$  catalyst at 150 °C and 250 °C. The chromatographic profiles confirm the formation of the same isomeric products at both

temperatures, although with different relative abundances. The two identified isomeric dimers were 2,4,4-trimethyl-1-pentene and 2,4,4-trimethyl-2-pentene. The trimerization pathway led to the formation of two isomeric  $C_{12}$  products: 2,2,6,6-trimethyl-4-methylene-heptane and 2,2,4,6,6-pentamethyl-3-heptene. Fig. S14 displays the relative distributions of these four main isomeric products at both reaction temperatures (150 °C and 250 °C) over the 3.7%  $W_{\text{SAC}}$  catalyst, under fixed gas hourly space velocity (GHSV) of 3000  $\text{h}^{-1}$  and weight hourly space velocity (WHSV) of 12 000  $\text{cm}^3 \text{g}^{-1} \text{h}^{-1}$  for 6 hours. The data reveal that the predominant  $C_8$  product at both temperatures was 2,4,4-trimethyl-1-pentene, accounting for 48.3% of total dimers at 150 °C and increasing to 59.2% at 250 °C. In contrast, the minor dimer isomer, 2,4,4-trimethyl-2-pentene, represented 18.8% and 35.1% at the respective temperatures. The increase in temperature from 150 °C to 250 °C enhanced the formation of both dimer products, with the major isomer showing a 22% increase and the minor isomer doubling in abundance (100% increase), indicating that elevated temperature promotes dimerization, particularly favoring the less thermodynamically stable or kinetically hindered isomer. In contrast, the formation of trimeric  $C_{12}$  olefins was significantly suppressed at a higher temperature. At 150 °C, the major trimer, 2,2,4,6,6-pentamethyl-3-heptene, constituted 20.8% of total products, while the minor trimer, 2,2,6,6-trimethyl-4-methylene-heptane, accounted for 14.1%. When the temperature was raised to 250 °C, these values dropped to 3.9% and 1.8%, respectively. This corresponds to suppression factors of approximately 81% and 87% for the major and minor trimer products. The data suggest that higher reaction temperatures disfavor trimerization, possibly due to enhanced desorption kinetics, increased competition for active sites, or thermal cracking of heavier oligomers. These findings underscore the strong temperature dependence of isobutene oligomerization pathways over the  $W_{\text{SAC}}/\text{SDA}$  catalysts. While higher temperatures promote dimer formation, particularly the more branched isomers, they concurrently suppress trimer formation, thereby enabling tunable product distributions based on process conditions. Such tunability is crucial for optimizing catalyst design and operating parameters in applications aiming at the selective production of liquid branched olefins for fuel or chemical feedstock use.

### Structure identification and product distribution from NMR analysis

The  $^1\text{H}$  NMR data of the six liquid samples obtained over the three different  $W_{\text{SAC}}/\text{SDA}$  catalyst compositions (1.6%, 3.7%, and 6%) at 150 °C and 250 °C are presented in Fig. S15–S20. The structures of the  $C_8$  and  $C_{12}$  products were determined using information contained in the NMR spectra. Initially, the HSQC cross-peaks were used to pair the  $^1\text{H}$  signals of hydrogens with the  $^{13}\text{C}$  signals of the carbons to which these



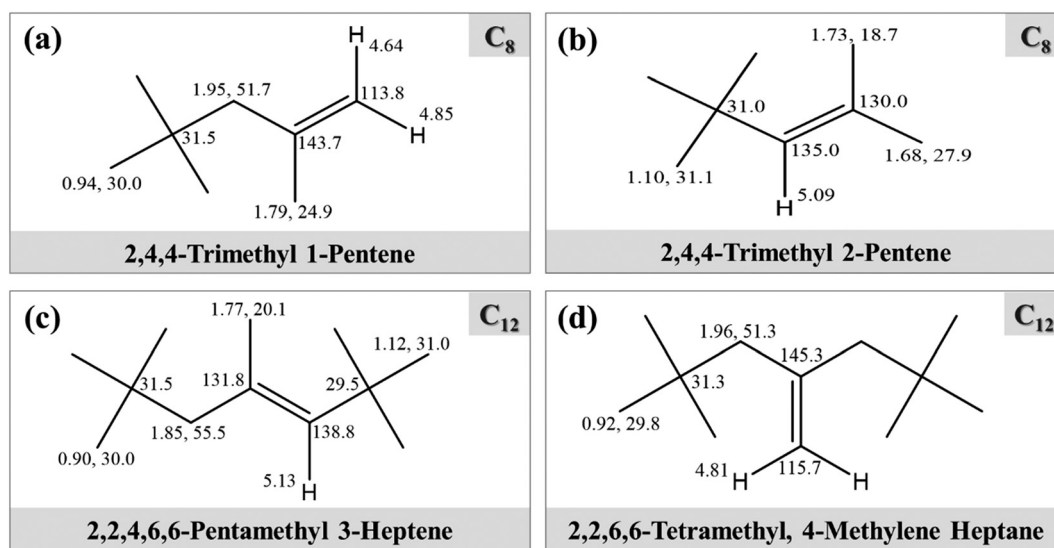
hydrogens were directly attached. Next, COSY correlations were used to pair  $^1\text{H}$  signals with one another, allowing the identification of which sets of  $^1\text{H}$  signals were generated by the same mixture component. Finally, HMBC cross peaks were used to correlate the  $^{13}\text{C}$  signals from non-protonated carbon sites with  $^1\text{H}$  signals from a particular component. Use of the intramolecular (through-bond) correlations found in the  $^1\text{H}$ - $^{13}\text{C}$  2D HSQC,  $^1\text{H}$ - $^1\text{H}$  2D COSY, and  $^1\text{H}$ - $^{13}\text{C}$  2D HMBC data sets, therefore, allowed all NMR signals to be grouped into component-specific subsets of the observed NMR signals. Having identified which signals arose from each component found in each mixture, the intensities (integrals) of the various  $^1\text{H}$  NMR signals were compared to determine how many hydrogens were responsible for the generation of each  $^1\text{H}$  NMR signal. Plausible chemical structures were either confirmed or refuted based on  $^1\text{H}$  and  $^{13}\text{C}$  chemical shifts and also based on the  $^1\text{H}$  signal intensities. In any case, where the NMR data disagreed with a proposed structure, a new structure was formulated that was consistent with observed data. The HMBC spectrum was particularly useful at this stage, as through-bond, heteronuclear NMR correlations allowed the identification of  $^{13}\text{C}$  signals from carbon sites two and three bonds removed from a given hydrogen. For  $^1\text{H}$ 's bound to  $\text{sp}^3$ -hybridized carbons, the HMBC spectrum contained cross peaks involving that  $^1\text{H}$  signal and  $^{13}\text{C}$  signals from carbon sites two and three bonds removed from the hydrogen, while for  $^1\text{H}$ 's bound to  $\text{sp}^2$ -hybridized carbons, the relative intensities of the HMBC cross peaks were used to differentiate between  $^{13}\text{C}$  signals that were *cis* versus *trans* (the *trans* three-bond couplings are larger than the *cis* three-bond couplings).

Fig. 10 displays the structures and chemical shifts of  $\text{C}_8$  and  $\text{C}_{12}$  olefin products obtained following isobutene conversion over different  $\text{W}_{\text{SAC}}/\text{SDA}$  catalysts, as determined

by NMR, including 2,4,4-trimethyl-1-pentene, 2,4,4-trimethyl-2-pentene, 2,2,4,6,6-pentamethyl-3-heptene, and 2,2,6,6-tetramethyl-4-methylene heptane. Fig. S21 displays the plots of selectivity as determined by NMR analysis for the different  $\text{C}_8$  and  $\text{C}_{12}$  olefin products including 2,4,4-trimethyl-1-pentene, 2,4,4-trimethyl-2-pentene, 2,2,4,6,6-pentamethyl-3-heptene, and 2,2,6,6-tetramethyl-4-methylene heptane obtained after 6 h of isobutene conversion over SDA-supported 1.6%, 3.7%, and 6%  $\text{W}_{\text{SAC}}$  catalysts at 150 °C and 250 °C under fixed GHSV and WHSV. At 150 °C, the 1.6%, 3.7%, and 6%  $\text{W}_{\text{SAC}}$  catalysts resulted in total  $\text{C}_8$  selectivity of 75%, 69%, and 89.8% compared to total  $\text{C}_{12}$  selectivity of 25%, 31%, and 10.2%, respectively. When the temperature increased to 250 °C, the 1.6%, 3.7%, and 6%  $\text{W}_{\text{SAC}}$  catalysts resulted in total  $\text{C}_8$  selectivity of 84.8%, 98%, and 96.5% compared to total  $\text{C}_{12}$  selectivity of 15.2%, 2%, and 3.5%, respectively.

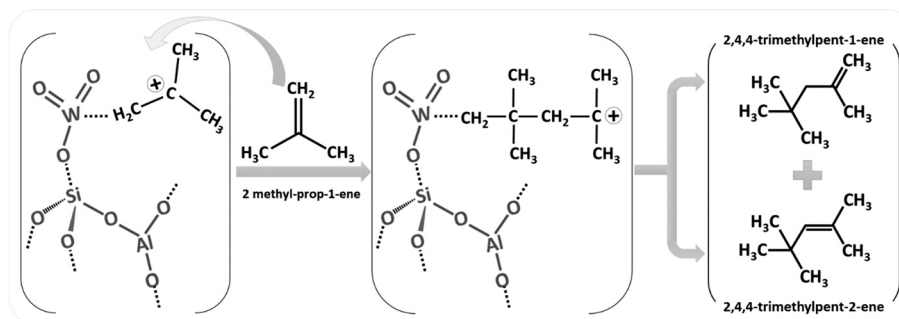
### Stability and reaction mechanism of $\text{W}_{\text{SAC}}/\text{SDA}$ catalysts

The long-term catalytic performance of the 3.7%  $\text{W}_{\text{SAC}}/\text{SDA}$  catalyst, which demonstrated the highest isobutene conversion and product selectivity among the studied catalysts, was evaluated through extended recyclability tests at 250 °C. Remarkably, the catalyst maintained consistent performance over more than 20 consecutive 6 h reaction cycles as well as over 5 prolonged reaction cycles of 48 h each. Across these tests, the percentage of isobutene conversion, selectivity toward  $\text{C}_8$  olefins, and total liquid product yield remained stable, highlighting the robustness of the catalyst under reaction conditions. Post-reaction characterization further supported these findings. XRD patterns and XPS spectra of the spent 3.7%  $\text{W}_{\text{SAC}}/\text{SDA}$  catalyst (Fig. S22) confirmed that neither the crystal structure nor the chemical composition of the catalyst had



**Fig. 10** Structures and chemical shifts of  $\text{C}_8$  and  $\text{C}_{12}$  olefin products as determined by NMR for (a) 2,4,4-trimethyl-1-pentene, (b) 2,4,4-trimethyl-2-pentene, (c) 2,2,4,6,6-pentamethyl-3-heptene, and (d) 2,2,6,6-tetramethyl-4-methylene heptane obtained from isobutene conversion over  $\text{W}_{\text{SAC}}/\text{SDA}$  catalysts.





**Scheme 2** Proposed mechanism for the dimerization of isobutene over the  $W_{SAC}/SDA$  catalysts.

deteriorated after extended catalytic use. These results demonstrate the structural and chemical integrity of the  $W_{SAC}/SDA$  system, validating its potential for long-term application in isobutene oligomerization.

Based on the combined insights from catalyst structure, spectroscopic analysis, and catalytic performance, a plausible mechanistic pathway for isobutene dimerization over the  $W_{SAC}/SDA$  catalyst is proposed as illustrated in Scheme 2.

The reaction is initiated through the coordination of an isobutene molecule to the catalytically active tungsten dioxo species, specifically the surface-bound  $-Si-O-W(=O)_2$  site. These active sites originate from the atomic dispersion of  $W_1-O_3$  moieties within the SDA support. Upon coordination, the isobutene undergoes electrophilic activation, forming a carbocation intermediate on the catalyst surface. A second isobutene molecule then acts as a nucleophile, attacking the surface-bound carbocation to form a  $C_8$  dimeric carbocation intermediate. This species subsequently undergoes a hydrogen atom transfer (hydride shift or proton loss) to yield a mixture of branched  $C_8$  olefins, primarily 2,4,4-trimethyl-1-pentene and 2,4,4-trimethyl-2-pentene.<sup>55</sup> The neutral  $C_8$  olefin products then desorb from the tungsten site, completing the catalytic cycle. Under appropriate conditions, the  $C_8$  olefins can undergo a second oligomerization step *via* a similar tungsten-mediated mechanism to form  $C_{12}$  products. In this subsequent step, the adsorbed  $C_8$  intermediate reacts with a third isobutene molecule, again proceeding through a carbocation intermediate and leading to the formation of isomeric  $C_{12}$  branched olefins. This proposed mechanism shows the critical role of isolated tungsten dioxo species in enabling the selective activation and transformation of isobutene molecules through a surface carbocation pathway. The confinement of  $W_{SAC}$  centers within the SDA matrix contributes not only to their atomic dispersion but also to their catalytic stability, enabling efficient and selective production of branched olefins over extended periods.

## Conclusions

The oligomerization of isobutene into  $C_8$  and  $C_{12}$  olefins presents a promising route to transform an underutilized light hydrocarbon into valuable, branched liquid fuels and chemical feedstocks. In this work, we developed an efficient

strategy to selectively convert isobutene into highly branched dimers and trimers using a novel tungsten single-atom catalyst ( $W_{SAC}$ ) system supported on silica-doped alumina (SDA). The  $W_{SAC}/SDA$  catalysts were synthesized through a straightforward approach involving the co-dispersion of Zn-BTC MOF and SDA in a hydroalcoholic medium, followed by pyrolysis at 1000 °C in an inert atmosphere and subsequent activation in static air at 700 °C. The Zn-MOF served as a sacrificial template, enabling the confinement and dispersion of isolated tungsten species within the SDA matrix. Structural characterization revealed atomically dispersed tungsten centers in the form of  $W_1-O_3$  moieties anchored on elongated SDA nanoparticles. Catalytic performance was evaluated under mild reaction conditions (1 atm, 150–250 °C) across a range of W loadings (1.6–6 wt%). The 1.6% and the 3.7%  $W_{SAC}/SDA$  samples exhibited single-atom catalyst features as confirmed using TEM, EXANES, and EXAFS analysis, in contrast to the sample with 6% W loading that did not exhibit a single-atom structure. The 3.7 wt%  $W_{SAC}/SDA$  catalyst demonstrated the most effective balance of activity and selectivity, achieving the highest isobutene conversion and liquid olefin production. Gas chromatography and NMR analyses confirmed the formation of two isomeric  $C_8$  dimers and two isomeric  $C_{12}$  trimers as the primary products. Moreover, product selectivity was strongly dependent on reaction temperature. At 150 °C, the liquid product consisted of ~60% dimers and ~40% trimers, whereas at 250 °C, selectivity shifted markedly toward dimers (~95%), with only ~5% trimers. These findings highlight the capability of  $W_{SAC}/SDA$  catalysts to enable tunable and selective oligomerization of isobutene through single-atom active sites. The excellent stability, high atomic dispersion, and catalytic control demonstrated by the 1.6–3.7%  $W_{SAC}/SDA$  system provide valuable insights for the rational design of next-generation single-atom catalysts for olefin upgrading. This work paves the way for efficient catalytic valorization of  $C_4$  hydrocarbons into branched liquid fuels and petrochemical intermediates under practical conditions.

## Author contributions

AFZ: conceptualization, experiments, and catalysis measurements. MM: NMR and ICP measurements. TB:





discussion of experiments and results. JHS: NMR analysis. SL and AAF: EXANES and EXAFS measurements and analysis. MSE: conceptualization, design and supervision of the project, discussion, manuscript editing and revision. All authors contributed to and approved the final version of the manuscript.

## Conflicts of interest

There are no conflicts to declare.

## Data availability

Supplementary information: XRD pattern of the Zn-BTC MOF; TEM images of the 5% SDA support; TEM images of the 1.6-6%  $W_{SAC}/SDA$  catalysts; TEM image of the 3.5%  $WO_3/SDA$  nanoparticle catalyst; plots for absorption edge energy ( $E_0$ ) determination, and fitting of the  $k^3$ -weighted FT of the EXAFS spectrum of the 3.7%  $W_{SAC}/SDA$  sample; fitting parameters for the  $k^3$ -weighted FT of the EXAFS spectra;  $H_2$ -TPR profiles of 5% SDA support and the 3.7%  $W_{SAC}/SDA$  catalyst;  $NH_3$ -TPD profiles of 5% SDA and various  $W_{SAC}/SDA$  catalysts; XPS spectra of the 3.5%  $WO_3/SDA$  catalyst; plots of isobutene conversion as a function of time over 1.6%, 3%, and 6%  $W_{SAC}/SDA$  catalysts at 150 °C and 250 °C; plots of product volume obtained for isobutene conversion as a function of tungsten loading after 6 h at 150 °C; plots of selectivity to  $C_8$  and  $C_{12}$  olefin products for isobutene conversion over 1.6%, 3.7%, and 6%  $W_{SAC}/SDA$  catalysts at 150 °C and 250 °C; gas chromatograms of liquid products formed after 6 h of isobutene conversion over the 3.7%  $W_{SAC}/SDA$  catalyst at 150 °C and 250 °C; plots of relative proportions for the  $C_8$  and  $C_{12}$  olefin products produced during isobutene conversion over 3.7%  $W_{SAC}/SDA$  at 150 °C and 250 °C;  $^1H$ - $^{13}C$  HMBC and HSQC spectra of 1.6%, 3.7%, and 6%  $W_{SAC}/SDA$  reaction products at 150 °C and 250 °C; plots of selectivity obtained by NMR analysis for  $C_8$  and  $C_{12}$  olefin products obtained after 6 h of isobutene conversion over 1.6%, 3.7%, and 6%  $W_{SAC}/SDA$  catalysts at 150 °C and 250 °C; XRD patterns of fresh and spent catalyst, and XPS spectra of the spent 3.7%  $W_{SAC}/SDA$  catalyst. See DOI: <https://doi.org/10.1039/D5CY00663E>.

The data supporting this article have been included as part of the SI.

## Acknowledgements

This work was supported by Shell Global Solutions under Grant Number CW759237 to Virginia Commonwealth University (VCU). The XAS measurements (by S. L. and A. A. F.) were performed at the beamline 12-BM of the Advanced Photon Source, a U.S. Department of Energy (DOE) Office of Science user facility at Argonne National Laboratory (ANL) and are supported by the U.S. DOE Office of Science-Basic Energy Sciences, under contract no. DE-AC02-06CH11357. We gratefully acknowledge Dr. Jinkyu Park (ANL) for their essential contributions to the XAS data analysis.

## References

- 1 A. Malaika, P. Rechia-Gorący, M. Kot and M. Kozłowski, *Catal. Today*, 2018, **301**, 266–273.
- 2 J. Saavedra Lopez, R. A. Dagle, V. L. Dagle, C. Smith and K. O. Albrecht, *Catal. Sci. Technol.*, 2019, **9**, 1117–1131.
- 3 J. Liu, Y. Ge, Y. Song, M. Du, X. Zhou and J. Wang, *Catal. Commun.*, 2019, **119**, 57–61.
- 4 E. Kocaman, Ö. Akarçay, N. Bağlar, S. Çelebi and A. Uzun, *Mol. Catal.*, 2018, **457**, 41–50.
- 5 D. H. Park, S.-S. Kim, T. J. Pinnavaia, F. Tzompantzi, J. Prince and J. S. Valente, *J. Phys. Chem. C*, 2011, **115**, 5809–5816.
- 6 F. Tzompantzi, M. Valverde-Herrera, J. Rodríguez-González, R. Gómez, A. Mantilla, J. L. Fernández and H. Ortiz, *Chem. Eng. Commun.*, 2009, **196**, 1198–1205.
- 7 B. Zhao, Y. Men, A. Zhang, J. Wang, R. He, W. An and S. Li, *Appl. Catal., A*, 2018, **558**, 150–160.
- 8 C. Larabi, A. Garron, P. Rouge, K. C. Szeto, S. Norsic, A. De Mallmann, N. Merle and M. Taoufik, *ChemCatChem*, 2017, **9**, 2160–2166.
- 9 J. Li, Z. Zhang, M. Cui, Q. Liu, Z. Fei, X. Chen, J. Tang and X. Qiao, *Catal. Commun.*, 2021, **148**, 106172.
- 10 Y. Yu, Z. Lv, H. Zhong, W. Bai and M. Ji, *Eur. J. Inorg. Chem.*, 2023, **26**, e202200631.
- 11 J. W. Yoon, J.-S. Chang, H.-D. Lee, T.-J. Kim and S. H. Jhung, *J. Mol. Catal. A: Chem.*, 2006, **260**, 181–186.
- 12 K. Hauge, E. Bergene, D. Chen, G. R. Fredriksen and A. Holmen, *Catal. Today*, 2005, **100**, 463–466.
- 13 D. Fritsch, I. Randjelovic and F. Keil, *Catal. Today*, 2004, **98**, 295–308.
- 14 J. W. Yoon, J.-S. Chang, H.-D. Lee, T.-J. Kim and S. H. Jhung, *J. Catal.*, 2007, **245**, 253–256.
- 15 X. Yu, Y. Liu, H. Wang, W. Cheng, Y. Wu and S. Zhang, *Mol. Catal.*, 2020, **482**, 110636.
- 16 A. Wassermann and W. T. Weller, *Nature*, 1942, **149**, 669.
- 17 A. Mantilla, G. Ferrat, A. López-Ortega, E. Romero, F. Tzompantzi, M. Torres, E. Ortiz-Islas and R. Gómez, *J. Mol. Catal. A: Chem.*, 2005, **228**, 333–338.
- 18 J. Li, M. Cui, Z. Zhang, X. Chen, Q. Liu, Z. Fei, J. Tang and X. Qiao, *Chin. J. Chem. Eng.*, 2021, **38**, 165–171.
- 19 A. Sarkar, D. Seth, M. Jiang, F. T. T. Ng and G. L. Rempel, *Top. Catal.*, 2014, **57**, 730–740.
- 20 J. S. Lee, J. W. Yoon, S. B. Halligudi, J.-S. Chang and S. H. Jhung, *Appl. Catal., A*, 2009, **366**, 299–303.
- 21 J. W. Yoon, S. H. Jhung, D. H. Choo, S. J. Lee and J.-S. Chang, *Chem. Lett.*, 2007, **36**, 1504–1505.
- 22 A. V. Lavrenov, T. R. Karpova, E. A. Buluchevskii and E. N. Bogdanets, *Catal. Ind.*, 2016, **8**, 316–327.
- 23 A. Corma, *Chem. Rev.*, 1997, **97**, 2373–2420.
- 24 Y. Chen, J. Zhao, X. Zhao, D. Wu, N. Zhang, J. Du, J. Zeng, X. Li, M. Salmeron, J. Liu and B. C. Gates, *Nat. Chem. Eng.*, 2025, **2**, 38–49.
- 25 Y. Zhao, Ö. D. Bozkurt, S. F. Kurtoglu-Öztulum, M. Su Yordanli, A. S. Hoffman, J. Hong, J. E. Perez-Aguilar, A. Saltuk, D. Akgül, O. Demircan, T. A. Ateşin, V. Aviyente, B. C. Gates, S. R. Bare and A. Uzun, *J. Catal.*, 2024, **429**, 115196.



- 26 K. Chen, J. Wang, H. Zhang, D. Ma and K. Chu, *Nano Lett.*, 2023, **23**, 1735–1742.
- 27 D. Yang, J. Wang, C. Lou, M. Li, C. Zhang, A. Ramon, C. Li, M. Tang, G. Henkelman, M. Xu, J. Li, J. Llorca, J. Arbiol, D. Mitlin, G. Zhou and A. Cabot, *ACS Energy Lett.*, 2024, **9**, 2083–2091.
- 28 D. A. Patel, G. Giannakakis, G. Yan, H. T. Ngan, P. Yu, R. T. Hannagan, P. L. Kress, J. Shan, P. Deshlahra, P. Sautet and E. C. H. Sykes, *ACS Catal.*, 2023, **13**, 4290–4303.
- 29 J. Sun, J. Yang, T. Wang, S. L. Zhang, H. Yuan, W. Zang, Y. Liu, X. Liu, W. Wang, S. Xi, C. H. Kirk, H. Wang, J. Wang, X. Wang, U. Bhat, Z. Liu, S. Wang, Y.-W. Zhang and J. Wang, *Nano Lett.*, 2024, **24**, 5206–5213.
- 30 M. Omran, T. Fabritius and E.-P. Heikkinen, *J. Sustain. Metall.*, 2019, **5**, 331–340.
- 31 K. Huang, C. Rong, W. Zhang, X. Yang, Y. Fan, L. Liu, Z. Yang, W. Chen and J. Yang, *Mater. Today Energy*, 2021, **19**, 100579.
- 32 G. Busca, *Catal. Today*, 2020, **357**, 621–629.
- 33 A. Sarkar, A. Adhikary, A. Mandal, T. Chakraborty and D. Das, *Cryst. Growth Des.*, 2020, **20**, 7833–7839.
- 34 A. Ghorbanian, S. Rowshanzamir and F. Mehri, *Sci. Rep.*, 2024, **14**, 14999.
- 35 A. Nowacka, P. Briantais, C. Prestipino and F. X. Llabrés i Xamena, *Cryst. Growth Des.*, 2019, **19**, 4981–4989.
- 36 E. Vyskočilová, L. Sekerová, I. Paterová, J. Krupka, M. Veselý and L. Červený, *J. Porous Mater.*, 2018, **25**, 273–281.
- 37 M. Lee, J. W. Yoon, Y. Kim, J. S. Yoon, H.-J. Chae, Y.-H. Han and D. W. Hwang, *Appl. Catal., A*, 2018, **562**, 87–93.
- 38 H. Jeong, T. W. Kim, M. Kim, G. B. Han, B. Jeong and Y.-W. Suh, *ACS Sustainable Chem. Eng.*, 2022, **10**, 15550–15563.
- 39 M. A. Adnan, O. Muraza, S. A. Razzak, M. M. Hossain and H. I. de Lasa, *Energy Fuels*, 2017, **31**, 7471–7481.
- 40 P. K. Dutta and B. Del Barco, *J. Phys. Chem.*, 1985, **89**, 1861–1865.
- 41 K. Ding, A. Gulec, A. M. Johnson, T. L. Drake, W. Wu, Y. Lin, E. Weitz, L. D. Marks and P. C. Stair, *ACS Catal.*, 2016, **6**, 5740–5746.
- 42 D. S. Kim, M. Ostromecki, I. E. Wachs, S. D. Kohler and J. G. Ekerdt, *Catal. Lett.*, 1995, **33**, 209–215.
- 43 I. Jonane, A. Anspoks and A. Kuzmin, *Modell. Simul. Mater. Sci. Eng.*, 2018, **26**, 025004.
- 44 Y. Feng, C. Wang, P. Cui, C. Li, B. Zhang, L. Gan, S. Zhang, X. Zhang, X. Zhou, Z. Sun, K. Wang, Y. Duan, H. Li, K. Zhou, H. Huang, A. Li, C. Zhuang, L. Wang, Z. Zhang and X. Han, *Adv. Mater.*, 2022, **34**, 2109074.
- 45 W. Chen, J. Pei, C.-T. He, J. Wan, H. Ren, Y. Wang, J. Dong, K. Wu, W.-C. Cheong, J. Mao, X. Zheng, W. Yan, Z. Zhuang, C. Chen, Q. Peng, D. Wang and Y. Li, *Adv. Mater.*, 2018, **30**, 1800396.
- 46 J. Finzel, K. M. Sanroman Gutierrez, A. S. Hoffman, J. Resasco, P. Christopher and S. R. Bare, *ACS Catal.*, 2023, **13**, 6462–6473.
- 47 J. L. Park, K. A. Canizales, M. D. Argyle, B. F. Woodfield and K. J. Stowers, *Microporous Mesoporous Mater.*, 2020, **293**, 109799.
- 48 A. N. T. Cao, D. H. Le Phuong, P. T. T. Phuong, T. H. Trinh, T. M. Nguyen and P. T. H. Pham, *Top. Catal.*, 2023, **66**, 247–261.
- 49 N. Li, Y. Zheng, L. Wei, H. Teng and J. Zhou, *Green Chem.*, 2017, **19**, 682–691.
- 50 A. F. Zedan, A. S. AlJaber and M. S. El-Shall, *ACS Omega*, 2022, **7**, 44021–44032.
- 51 M. B. Gongalsky, J. V. Kargina, J. F. Cruz, J. F. Sánchez-Royo, V. S. Chirvony, L. A. Osminkina and M. J. Sailor, *Front. Chem.*, 2019, **7**, 165, DOI: [10.3389/fchem.2019.00165](https://doi.org/10.3389/fchem.2019.00165).
- 52 D. I. Miakota, R. R. Unocic, F. Bertoldo, G. Ghimire, S. Engberg, D. Geohegan, K. S. Thygesen and S. Canulescu, *Nanoscale*, 2022, **14**, 9485–9497.
- 53 Y. Gu, T. Xu, Z. Zhu, X. Chen, W. Chen and W. Lu, *ACS Appl. Mater. Interfaces*, 2021, **13**, 37142–37151.
- 54 L. Díaz-Ballote, E. T. Vega-Lizama, L. M. López and W. S. González-Gómez, *J. Solid State Electrochem.*, 2024, **28**, 3905–3914.
- 55 N. Maity, S. Barman, Y. Minenkov, S. Ould-Chikh, E. Abou-Hamad, T. Ma, Z. S. Qureshi, L. Cavallo, V. D'Elia, B. C. Gates and J.-M. Basset, *ACS Catal.*, 2018, **8**, 2715–2729.

